Paper I

Journal of
METAMORPHIC GEOLOGY

J. metamorphic Geol., 2015, **33,** 513–534 doi:10.1111/jmg.12131

Behaviour of geochronometers and timing of metamorphic reactions during deformation at lower crustal conditions: phase equilibrium modelling and U–Pb dating of zircon, monazite, rutile and titanite from the Kalak Nappe Complex, northern Norway

D. GASSER,[1] P. JEŘÁBEK,[2] C. FABER,[3] H. STÜNITZ,[3] L. MENEGON,[4] F. CORFU,[5] M. ERAMBERT[5] AND M. J. WHITEHOUSE[6]

[1]*Geological Survey of Norway, Leiv Eirikssons vei 39, 7491 Trondheim, Norway (deta.gasser@ngu.no)*
[2]*Institute of Petrology and Structural Geology, Charles University, 128 43 Praha 2, Czech Republic*
[3]*Department of Geology, University of Tromsø, Dramsveien 201, 9037 Tromsø, Norway*
[4]*School of Geography, Earth and Environmental Sciences, Plymouth University, Fitzroy, Drake Circus, Plymouth, Devon PL4 8AA, UK*
[5]*Department of Geosciences, University of Oslo, Postbox 1047, Blindern, 0316 Oslo, Norway*
[6]*Department of Geosciences, Swedish Museum of Natural History, Box 50007, SE-104 05 Stockholm, Sweden*

ABSTRACT This study investigates the behaviour of the geochronometers zircon, monazite, rutile and titanite in polyphase lower crustal rocks of the Kalak Nappe Complex, northern Norway. A pressure–temperature–time–deformation path is constructed by combining microstructural observations with *P–T* conditions derived from phase equilibrium modelling and U–Pb dating. The following tectono-metamorphic evolution is deduced: A subvertical S1 fabric formed at ~730–775 °C and ~6.3–9.8 kbar, above the wet solidus in the sillimanite and kyanite stability fields. The event is dated at 702 ± 5 Ma by high-U zircon in a leucosome. Monazite grains that grew in the S1 fabric show surprisingly little variation in chemical composition compared to a large spread in (concordant) U–Pb dates from *c*. 800 to 600 Ma. This age spread could either represent protracted growth of monazite during high-grade metamorphism, or represent partially reset ages due to high-*T* diffusion. Both cases imply that elevated temperatures of >600 °C persisted for over *c*. 200 Ma, indicating relatively static conditions at lower crustal levels for most of the Neoproterozoic. The S1 fabric was overprinted by a subhorizontal S2 fabric, which formed at ~600–660 °C and ~10–12 kbar. Rutile that originally grew during the S1-forming event lost its Zr-in-rutile and U–Pb signatures during the S2-forming event. It records Zr-in-rutile temperatures of 550–660 °C and Caledonian ages of 440–420 Ma. Titanite grew at the expense of rutile at slightly lower temperatures of ~550 °C during ongoing S2 deformation; U–Pb ages of *c*. 440–430 Ma date its crystallization, giving a minimum estimate for the age of Caledonian metamorphism and the duration of Caledonian shearing. This study shows that (i) monazite can have a large spread in U–Pb dates despite a homogeneous composition; (ii) rutile may lose its Zr-in-rutile and U–Pb signature during an amphibolite facies overprint; and (iii) titanite may record crystallization ages during retrograde shearing. Therefore, in order to correctly interpret U–Pb ages from different geochronometers in a polyphase deformation and reaction history, they are ideally combined with microstructural observations and phase equilibrium modelling to derive a complete *P–T–t–d* path.

Key words: Kalak Nappe Complex; monazite; phase equilibrium modelling; rutile; titanite; U–Pb dating; zircon.

INTRODUCTION

The correct assembly of pressure–temperature–time–deformation (*P–T–t–d*) paths in polymetamorphic rocks is crucial for reconstructing the tectonic history of orogens and for constraining large-scale tectonic models. However, linking metamorphic and structural records to specific points in *P–T–t* space is difficult. It requires a thorough understanding of the microstructural links between metamorphic reactions, deformation and the chemical processes involved in the formation and crystallization, modification and destruction of datable minerals such as zircon, monazite, rutile or titanite (e.g. Müller, 2003; Gibson

et al., 2004). One approach is to couple a *P–T* path obtained by various thermobarometric methods from major phases with the compositional patterns of major and trace elements in accessory phases used for dating (e.g. Rubatto, 2002; Gibson *et al.*, 2004; Slàma *et al.*, 2007; Williams *et al.*, 2007). Alternatively, the *P–T* path obtained from major phases can be combined with the results of geothermobarometry, directly involving the dated accessory minerals, e.g. Ti-in-zircon thermometry (e.g. Watson & Harrison, 2005; Watson *et al.*, 2006), monazite-garnet thermometry (e.g. Pyle *et al.*, 2001), Zr-in-rutile thermometry (Zack *et al.*, 2004; Watson *et al.*, 2006; Tomkins *et al.*, 2007) or Zr-in-titanite thermobarometry (Hayden *et al.*, 2008). The connection between mineral reactions and deformation is then made by identifying the mineral assemblage as syn- or post-deformational using microstructural criteria. So provided that the formation of the dated minerals can be connected with the metamorphic reactions, it is possible to establish an absolute time sequence for tectonic processes by carefully analysing the deformation and reaction microstructures and dating selected minerals.

In this contribution we present a case study from metapelitic rocks of the Kalak Nappe Complex (KNC) of northern Norway that experienced polyphase deformation and metamorphism under lower crustal conditions. The KNC is part of a major nappe stack within the Caledonian orogen of Scandinavia. It was originally interpreted to represent the telescoped Neoproterozoic passive margin of the Baltican shield (e.g. Sturt *et al.*, 1978). More recent studies have revealed a complex Neoproterozoic tectonometamorphic evolution, which appears to be atypical for the western Baltica margin, and new models deriving the KNC from Laurentia, Siberia or peri-Gondwana have been proposed (e.g. Corfu *et al.*, 2007, 2011; Kirkland *et al.*, 2007a, b). Most of these models are based on U–Pb dating of detrital zircon as well as U–Pb dating of intrusive bodies and leucosomes. Information about the conditions and timing of metamorphism and deformation of the KNC is rare.

Two distinct deformation fabrics are investigated in the metapelitic rocks, and the observed microstructures are related to *P–T* conditions obtained from phase equilibrium modelling of major phases and Zr-in-rutile thermometry, as well as to U–Pb ages of zircon, monazite, rutile and titanite. The data set provides constraints on the structural, metamorphic and temporal evolution of the upper part of the KNC and allows further insights into the behaviour of the U–Pb geochronometers zircon, monazite, rutile and titanite within a polyphase deformed and metamorphosed lower crustal sequence.

GEOLOGICAL FRAMEWORK OF THE KNC

The KNC occupies large parts of the Troms and Finnmark counties in northern Norway (Fig. 1). It overlies the Gaissa and Laksefjord nappe complexes and is in turn overlain by the Magerøy/Reisa Nappe Complex (Fig. 1). The KNC consists of several distinct thrust sheets that are mainly composed of thick sequences of psammitic and pelitic metasedimentary gneisses with minor marbles as well as mafic to felsic intrusions (Fig. 1; e.g. Ramsay *et al.*, 1985).

The oldest rocks so far identified within the KNC are represented by the Fagervik complex, which consists of paragneisses deposited after 1948 ± 17 Ma, intruded by a 1796 ± 3 Ma granite (Kirkland *et al.*, 2008b). The paragneisses in the lower nappes of the KNC are attributed to the Sværholt succession, which is dominated by sedimentary rocks deposited at *c.* 1030–980 Ma, and deformed, metamorphosed and intruded by granitic plutons at *c.* 980–960 Ma (Fig. 1; Kirkland *et al.*, 2006a, 2007b, 2008b; Corfu *et al.*, 2011). The paragneisses in the upper nappes of the KNC are attributed to the Sørøy succession, which has a depositional age of *c.* 910–840 Ma and was deformed, metamorphosed and intruded by granitic plutons at *c.* 850–820 and *c.* 710 Ma (Kirkland *et al.*, 2006a, 2007b, 2008b; Corfu *et al.*, 2007, 2011). In addition, the Sørøy succession is intruded by *c.* 580–520 Ma mafic rocks of the Seiland Igneous Province (SIP, Fig. 1; Roberts *et al.*, 2006, 2010). The uppermost units of the KNC, found on Sørøya, consist of limestones and pelites (the Falkenes limestone and Åfjord pelites) and have a depositional age of *c.* 760–710 Ma (Fig. 1; Slagstad *et al.*, 2006). The youngest intrusive rocks within the KNC are *c.* 450–420 Ma pegmatites and granitic veinlets (Kirkland *et al.*, 2007a, 2009; Corfu *et al.*, 2011). The original relationship between the Fagervik complex and the younger Sværholt and Sørøy successions is unclear, as they are all separated by tectonic contacts. Within the southern and southwestern parts of the KNC, south and east of the Alta window, various para- and orthogneisses of unknown age and origin occur (Fig. 1).

The timing of thrusting and structural assembly of the KNC has been much debated and is not fully resolved. Originally, a two-stage Caledonian evolution was proposed (e.g. Sturt *et al.*, 1978). However, a more complex evolution involving several Neoproterozoic deformation and metamorphic events is now evident (e.g. Daly *et al.*, 1991; Kirkland *et al.*, 2006a; Corfu *et al.*, 2011; Menegon *et al.*, 2011). This indicates that the KNC consists of a complex pre-Caledonian basement nappe stack that was pervasively overprinted and reworked during the Caledonian orogeny.

THE EIDET LOCALITY

The metapelitic rocks investigated in this study are located at the southwestern end of the KNC, along a ~23 km long peninsula stretching northwards from the mainland (Fig. 1). The southern part of the

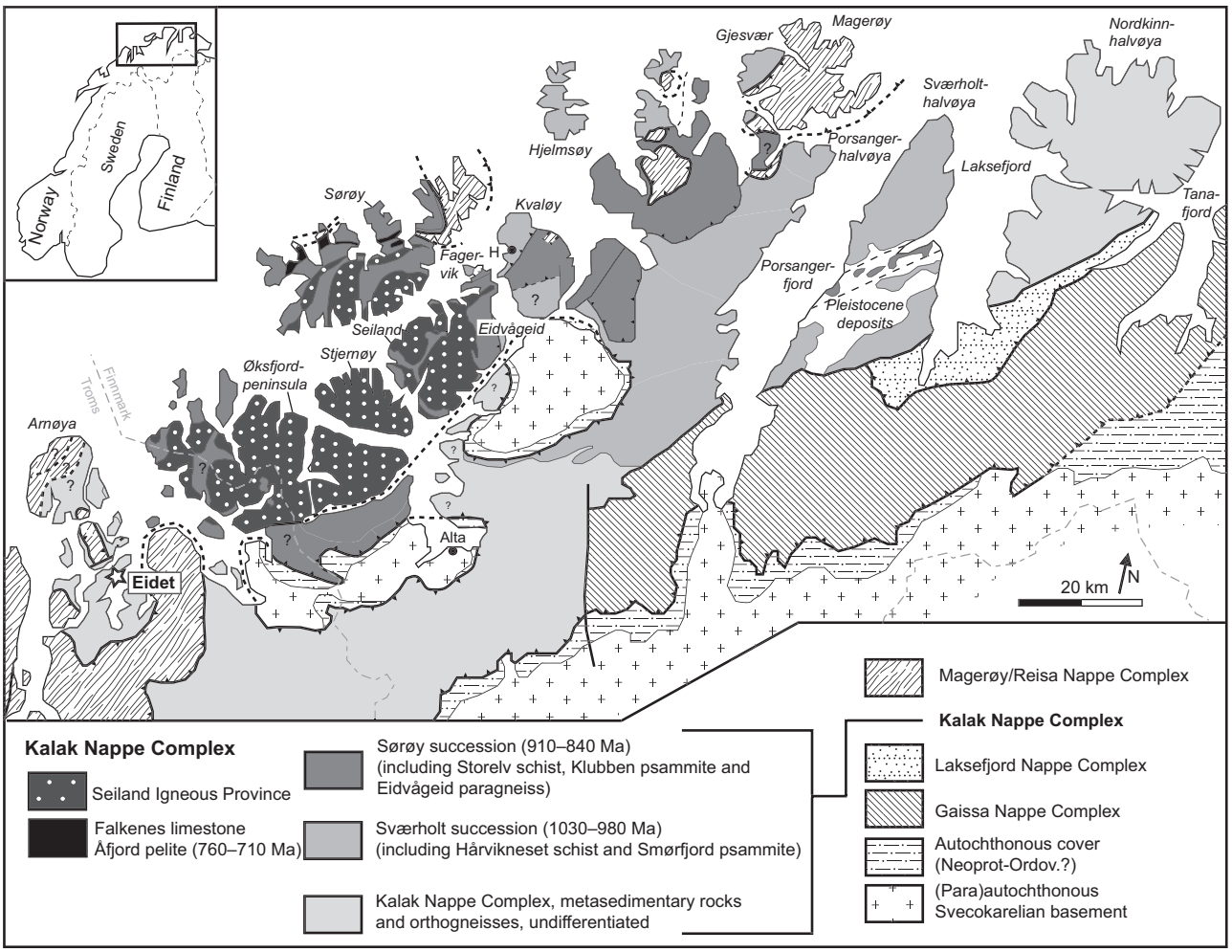

Fig. 1. Geological map of the Kalak Nappe Complex, showing the location of the Eidet locality in the southwest (map modified from Zwaan, 1988; Kirkland *et al.*, 2007b, 2008b). H, Hammerfest.

peninsula consists of granodioritic gneiss of unknown age, and the northern part of alternating and highly sheared psammitic, pelitic, pegmatitic and amphibolitic rocks (Zwaan, 1988). These mainly metasedimentary rocks have so far not been attributed to the Sværholt or Sørøy successions defined farther north (Fig. 1). The main fabric on the peninsula is a subhorizontal, penetrative metamorphic foliation, which is attributed to Caledonian shearing.

In several places, however, an older subvertical fabric has been observed within lens-shaped domains several metres in size. Although 'fabric' refers mainly to the foliation, it includes other aspects of the microstructure as well: lineation, shape and crystallographic preferred orientation of minerals, etc. One important aspect of the term 'fabric', here, is that it includes a particular mineral assemblage, which can be associated with these fabric elements. The older subvertical fabric, here termed S1, is typically overprinted and surrounded by the dominant subhorizontal fabric, here termed S2. Such an S1-lens is well exposed at the Eidet locality, a ~100 m long road cut within the metasedimentary sequence (Fig. 2a,b). Most of the outcrop is dominated by the S2 fabric, with an ~10 m wide zone of S1 fabric in its central part (Fig. 2a). The S1 fabric trends NW–SE and has no clear associated stretching lineation (Fig. 2a). Leucocratic material occurs as layers and patches parallel to the S1 fabric (Fig. 2b–d). The S2 fabric dips gently towards SW- or NE and bears a strong SE- or NW-plunging intersection and stretching lineation (Fig. 2a). Feldspathic sigma clasts indicate a top-to-the-southeast shear sense associated with this lineation.

From the field observations it is evident that the mineral assemblage defining the S1 fabric records higher grade metamorphism (e.g. partial melting represented by leucosome layers and lenses) than the mineral assemblage defining the S2 fabric (e.g. widespread muscovite parallel to foliation and no evidence for partial melting coeval with shearing). In order to decipher the metamorphic grade and date

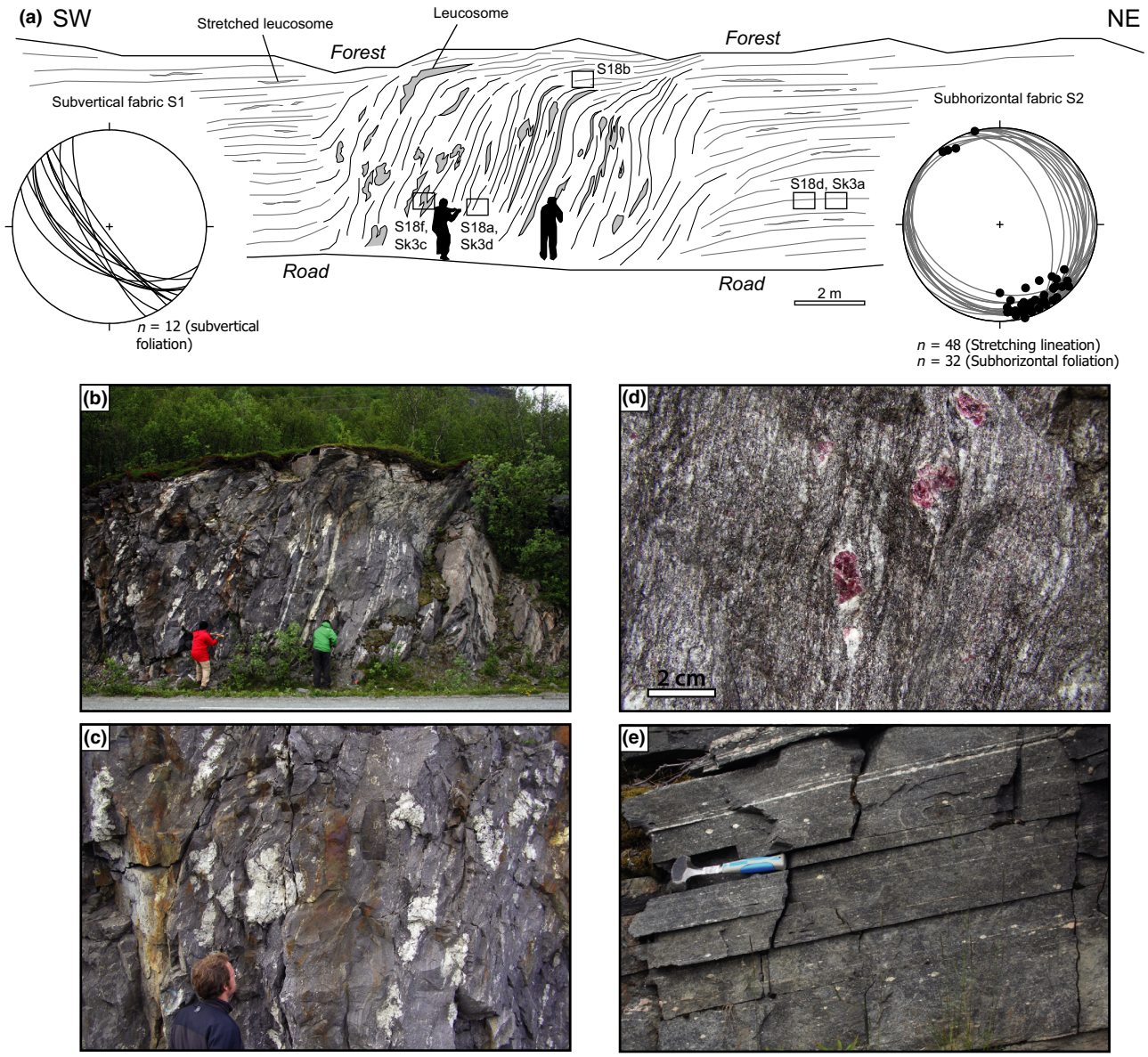

Fig. 2. Field relationships at the Eidet locality. (a) Sketch of the road cut close to Eidet (N69.904317/E20.947667). The subvertical, leucosome-bearing S1 fabric is preserved within a ~10 m wide lens surrounded by the subhorizontal S2 fabric. Stereoplots are equal area projections produced with the Stereo32-software. The locations of the petrological (S18a, b, f, d) and geochronological (Sk3a, c, d) samples are shown. Note that the road cut is oriented perpendicular to the dominant NW–SE-striking stretching lineation on the subhorizontal fabric. (b) Photograph of the S1 fabric within the Eidet lens. Persons for scale. (c) Photograph of the leucosome layers and boudins within the S1 fabric. Person for scale. (d) Garnet within small leucosome patches of the S1 fabric. (e) Photograph of the S2 fabric showing highly sheared and disintegrated leucosome layers. Hammer for scale.

these two contrasting fabrics, several samples were collected from the leucocratic lenses, the S1 fabric, and the S2 fabric (Fig. 2a; Table 1). It was attempted to trace the earlier S1 fabric into the overprinting S2 fabric in order to sample similar bulk rock compositions. Whole-rock chemistry revealed metapelitic compositions with comparable element proportions in all analysed samples (Table 2). Mineral abbreviations follow Kretz (1983). A description of the analytical methods can be found in Appendix S1.

Petrography and mineral chemistry of the subvertical S1 fabric

Four samples from the migmatitic S1 fabric were investigated in detail: S18f and Sk3c from leucosomes, and S18a and Sk3d from melanosomes (Fig. 2a; Table 1). The leucosomes consist of quartz, plagioclase and K-feldspar (partly replaced by myrmekites; Fig. 3a) and are frequently associated with large (up to 5 cm in size) garnet porphyroblasts

Table 1. Mineral assemblages for each sample and applied methods.

	Main minerals								Accessory minerals							
	Bt	Pl	Qtz	Grt	Kfs	Sil	Ky	Ms	Zrn	Mnz	Rt	Ttn	Ill	Ap	Ep/Aln	Methods
Subvertical fabric																
S18a	x	x	x	x	x	x	x	x	x	x	x			x		Petrology
Sk3c	x	x	x	x	x	x			x	x	x			x		Petrology, zircon, monazite, rutile dating, rutile thermometry
S18f	x	x	x	x	x	x	x	x	x	x	x			x		Petrology, phase equilibrium modelling
Sk3d	x	x	x	x	x	x	x	x								Petrology, monazite, rutile dating, rutile thermometry
Subhorizontal fabric																
S18b	x	x	x	x		x		x	x		x	x	x	x	x	Petrology, phase equilibrium modelling
S18d	x	x	x	x		x		x	x		x	x	x	x	x	Petrology
Sk3a	x	x	x	x				x	x		x	x	x	x	x	Petrology, rutile, titanite dating, detrital zircon dating

Table 2. Representative bulk rock compositions.

	S1		S2	
Sample	S18a	S18f	S18b	S18d
wt%				
SiO_2	61.50	61.50	62.70	61.80
TiO_2	1.05	1.08	1.07	0.83
Al_2O_3	18.80	18.70	17.20	16.20
Fe_2O_3	0.75	0.79	0.68	0.58
FeO	6.74	7.13	6.12	5.19
MnO	0.16	0.14	0.11	0.10
MgO	2.03	2.16	1.88	1.67
CaO	1.70	1.35	2.09	1.35
Na_2O	2.01	1.79	3.20	2.17
K_2O	3.47	3.76	3.12	3.91
P_2O_5	0.21	0.10	0.12	0.10
H_2O	1.57	1.46	1.66	6.14
Total	99.99	99.96	99.95	100.04

(Figs 2d & 3a–c). In the melanosomes, the garnet porphyroblasts are usually smaller (up to 2 mm in size) and surrounded by a medium-grained matrix of biotite, plagioclase, quartz, sillimanite and minor muscovite (Fig. 3d–f). Sillimanite is abundant and occurs as fine-grained laths and mats intergrown with biotite and minor muscovite mostly subparallel to S1 (Fig. 3c,e). In some places, it appears to be overgrown by kyanite, and in others it appears to overgrow the kyanite together with muscovite. Kyanite occurs as large crystals along the outer edge of leucosomes or intergrown with biotite (Fig. 3b,c,e). The kyanite is mostly elongated parallel to the S1 fabric, but some grains have random orientations. Rutile is relatively abundant, and occurs as elongated crystals parallel to the S1 fabric (Fig. 3f). Garnet is usually idiomorphic and contains inclusions of biotite, muscovite, quartz, sillimanite and zircon (Fig. 3). It shows a relatively flat compositional profile in the core (Grt I), followed by a transition zone and thin idiomorphic edges (Grt II) with higher Ca and lower Mn contents (Table S1; Fig. 4a).

Petrography and mineral chemistry of the subhorizontal S2 fabric

Three samples from the S2 fabric were investigated (Fig. 2a). The samples typically show relict S1 overprinted by S2, with S18b being the least and S18d and Sk3a the most overprinted samples (Fig. 2a). Compared to the S1 fabric, the S2 fabric is characterized by a finer grained matrix containing quartz, plagioclase, muscovite and biotite, as well as porphyroblasts of garnet (Fig. 5a,b). Aluminosilicates and K-feldspar are absent from the matrix of all these samples (Table 1), but garnet I cores in samples S18b and S18d contain inclusions of sillimanite (Fig. 5c). Myrmekite microstructures in the matrix of sample Sk3a suggest the former presence of K-feldspar. Epidote/allanite occurs as small, fabric-parallel elongate grains, whereas monazite is absent from all S2 fabric samples. Titanite is abundant and occurs as elongated grains parallel to the S2 fabric, or as coronas around rutile and/or ilmenite (Fig. 5d). Garnet in the S2 fabric again shows two compositionally distinct varieties, Grt I and Grt II, separated by a transition zone (Fig. 4b–d). In sample S18b, Grt II rims are negligible in leucosomes and more pronounced in the matrix (Fig. 4b,c). The Grt I cores in the S2 fabric show significantly greater compositional variation than in the S1 fabric, whereas the composition of Grt II in the S2 fabric is comparable to that of Grt II in the S1 fabric (Table S1; Fig. 4).

P–T RESULTS

In order to estimate *P–T* conditions of both fabrics, phase equilibrium modelling was applied with Perple_X (Connolly, 2005: version 6.6.6) using the internally consistent thermodynamic data set of Holland & Powell (1998: 2004 upgrade). Whole-rock compositions of the four petrological samples are similar (Table 2) indicating that the observed mineral assemblages have formed from a similar starting material. The only exception is the water content in the most overprinted sample S18d, which is significantly higher due to the increased proportion of matrix muscovite (Table 2). Based on the observed mineralogy and mineral chemistry, samples S18f and S18b were used to estimate *P–T* conditions of S1. In addition, S18b was used to estimate *P–T* conditions of S2. The calculations were performed in the MnNCKFMASHTi system using the XRF whole-rock compositions listed

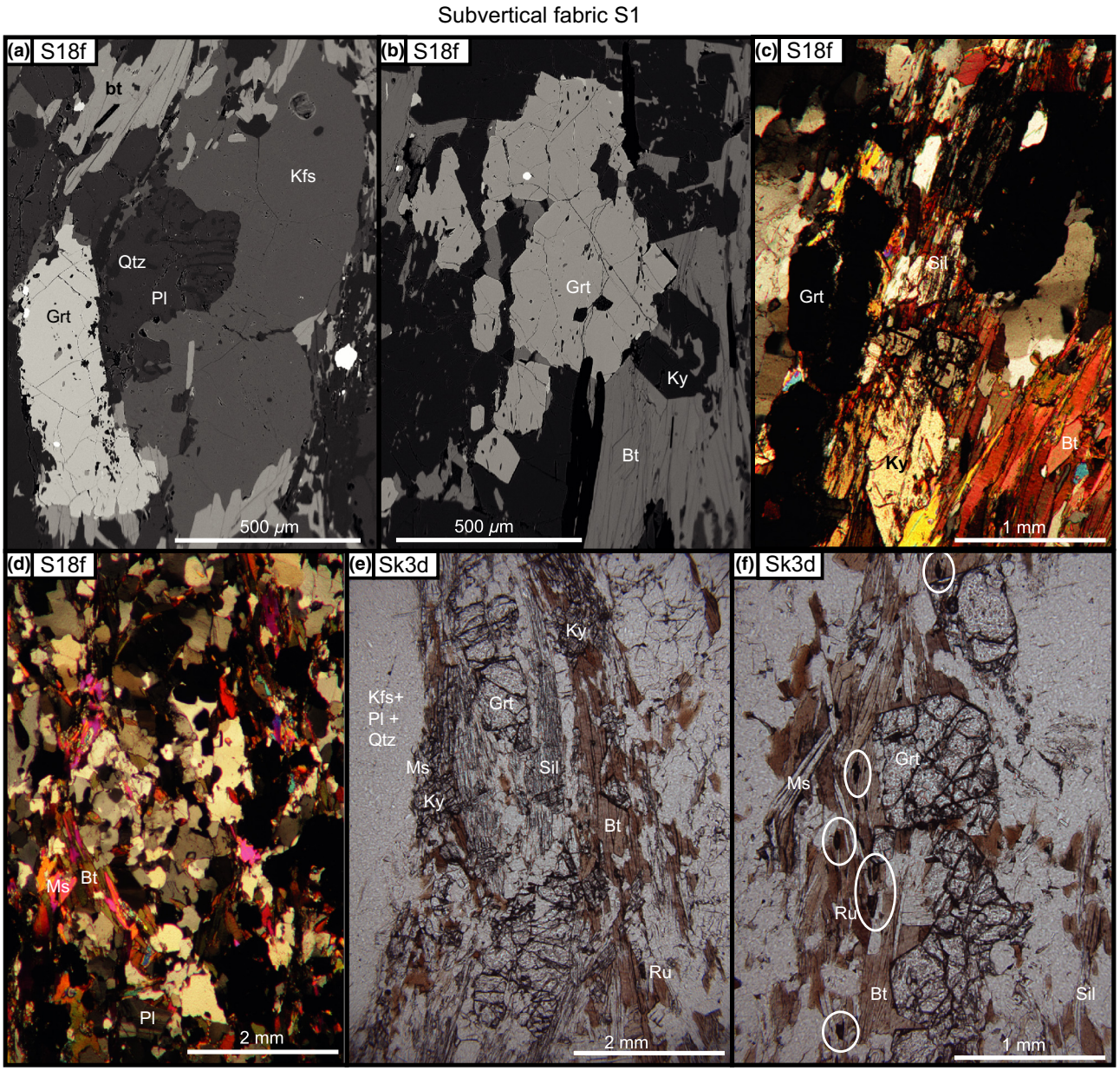

Fig. 3. Back-scatter electron (BSE) and light microscopy images of the S1 fabric. (a) BSE image showing garnet associated with S1 leucosome containing myrmekite and K-feldspar. (b) BSE image showing kyanite associated with garnet and biotite. (c) Photomicrograph showing sillimanite overgrowing kyanite. (d) Photomicrograph of typical S1 fabric defined weakly by biotite, muscovite and quartz-feldspar aggregate lenses (melt). (e) Photomicrograph showing S1-foliation-parallel sillimanite, kyanite and biotite. (f) Thin section photograph showing the presence of S1-foliation-parallel rutile crystals.

in Table 2 and shown in Fig. 6. The fluid in the calculations was taken from loss on ignition and regarded as a pure phase. The following solution mixing models were used: garnet (Holland & Powell, 1998), biotite (Tajčmanová *et al.*, 2009), white mica (Coggon & Holland, 2002), ternary feldspar (Fuhrman & Lindsley, 1988) and melt (Holland & Powell, 2001). The resulting pseudosections are presented in Fig. 6. Measured chemical compositions of minerals in question that are compared with isopleths in pseudosections can be found in Tables S1 and S2 and Fig. 4. The used values of X_{Mg} = Mg/Mg + Fe_{tot} and An = Ca/Ca + Na + K.

Phase equilibrium modelling results

Despite minor overprint by S2, sample S18f is dominated by the S1 assemblage GrtI–Bt–Kfs–Plg–Qtz–Ky–Sill, which according to the calculated pseudosection is stable above the solidus at

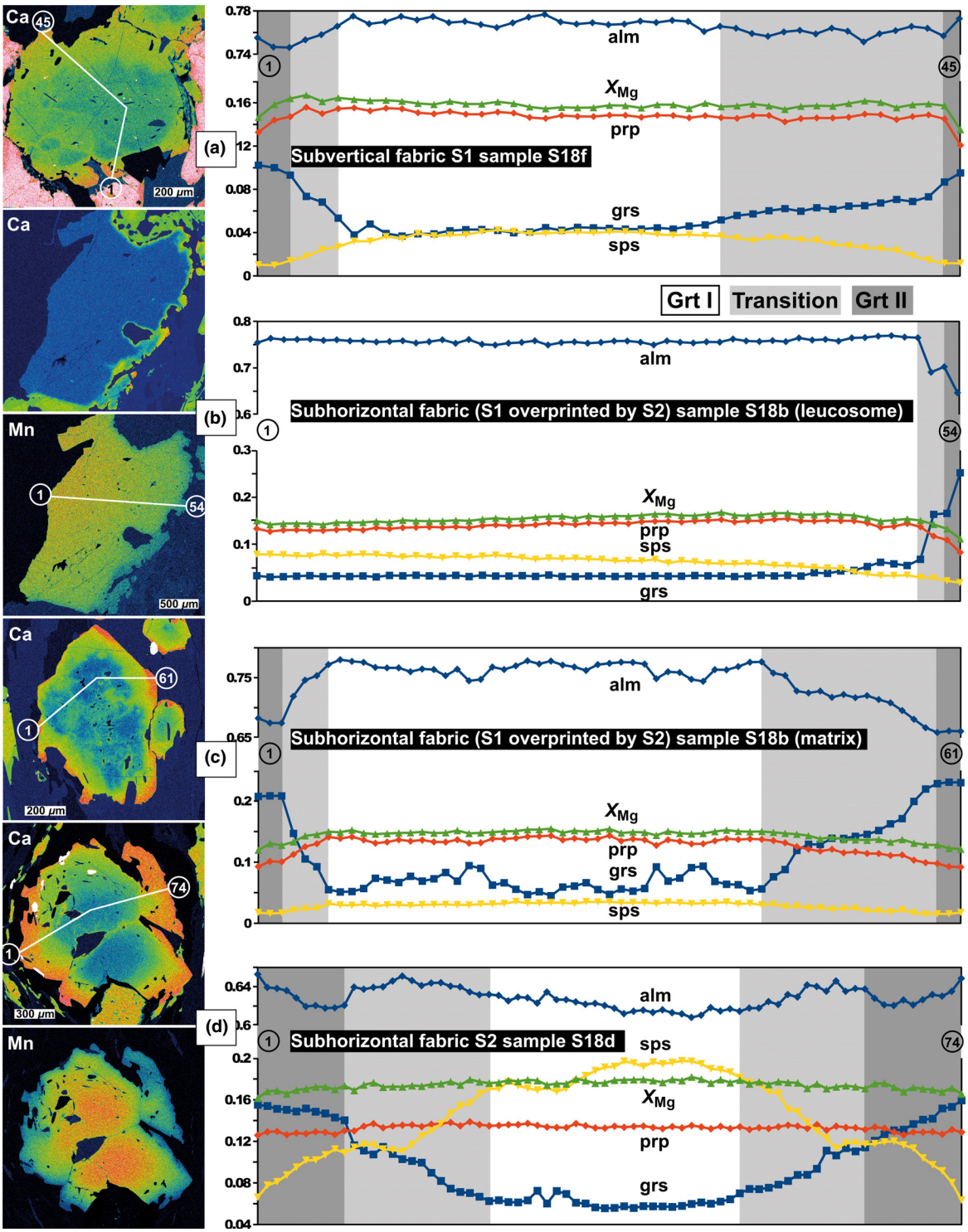

Fig. 4. Garnet profiles. (a) Profile across grain in S1 sample S18f (number of points, n = 44). (b) and (c) Profiles across grains from the leucosome (b) and the matrix (c) in S2 sample S18b (n = 54 and 61 respectively). (d) Profile across grain from S2 sample S18d (n = 74).

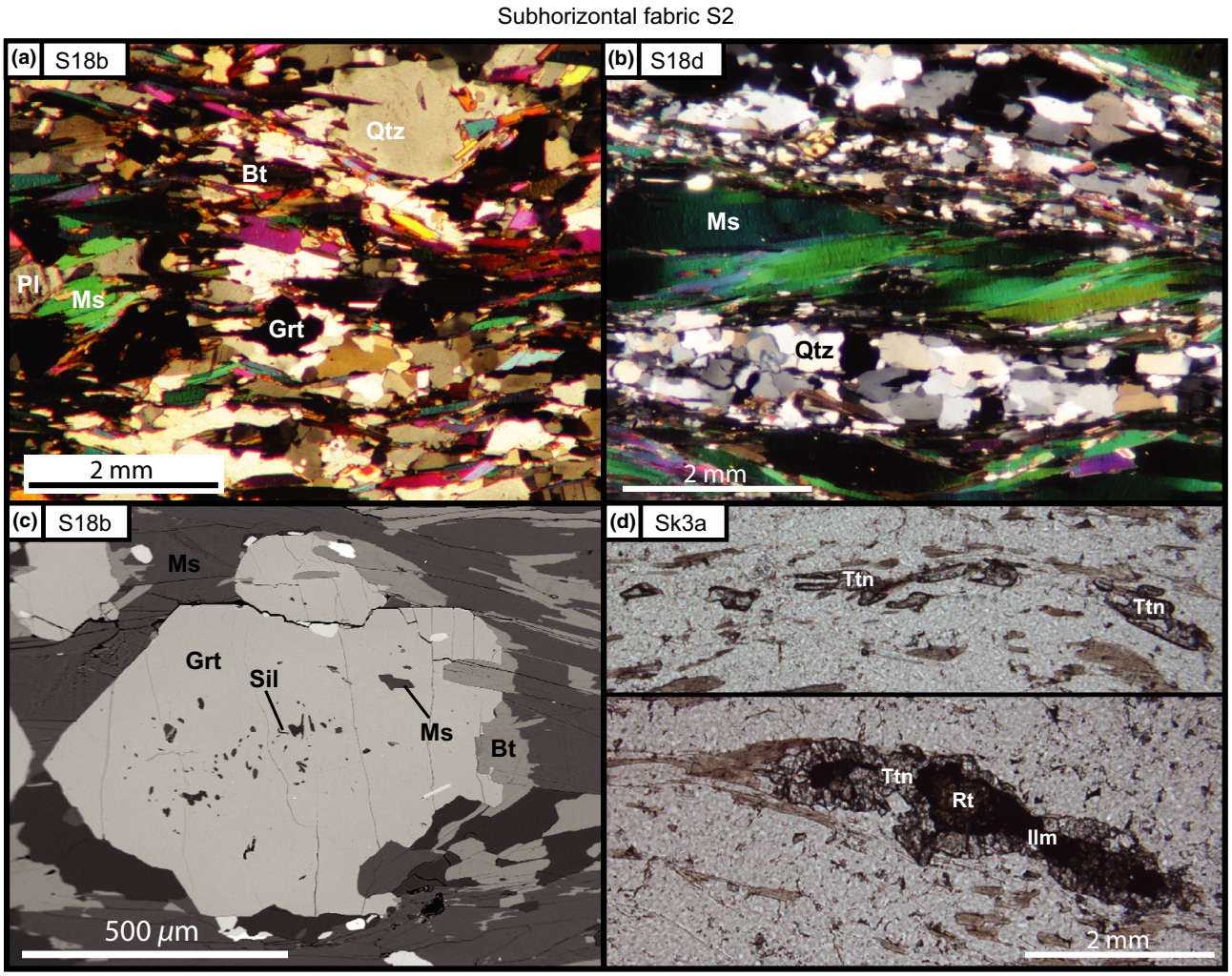

Fig. 5. BSE and light microscopy images of the S2 fabric. (a) Photomicrograph of sample S18b showing the S2 fabric defined by biotite, muscovite and elongate quartz aggregates. (b) Photomicrograph of sample S18d showing complete overprint by the S2 fabric defined by quartz-aggregate layers and lenses and muscovite fish. (c) BSE image showing sillimanite and muscovite inclusions in a garnet in sample S18b. (d) Photomicrographs of titanite aligned parallel to the S2 fabric. In some cases, titanite overgrows rutile and/or ilmenite.

~750–840 °C (Fig. 6a). The compositional isopleth X_{Mg} 0.16–0.17 of garnet I (Fig. 4a; Table S1) constrains the temperature to 750–775 °C. In this range, the grossular component of 4–7 mol.% indicates pressures of ~6.3–9.8 kbar, crossing the ky/sill univariant reaction curve (grey box in Fig. 6a). The microstructural relationship between kyanite and sillimanite is ambiguous, with sillimanite appearing as inclusions in garnet I, and also to both replace and be replaced by kyanite. This may either indicate (i) *P–T* conditions close to the ky/sill univariant reaction curve at ~8.5–9.75 kbar or (ii) sillimanite was stable before and after peak kyanite formation. Both early sillimanite and kyanite are associated with melt patches, but the peak assemblage for melting involves kyanite, and therefore the peak *P–T* estimates can be constrained to 760–775 °C and 8.8–9.8 kbar (light grey box in Fig. 6a). The isopleth for the spessartine component of ~4 mol.% in garnet I occurs near this estimated *P–T* range at slightly higher temperatures or pressures (Fig. 6a). The isopleths of An ~0.28–0.29 in plagioclase and Ti (a.p.f.u.) ~0.23–0.28 in biotite for the estimated *P–T* range are compatible with measured compositions of these minerals (Table S2). In contrast, the measured X_{Mg} of 0.44–0.53 in biotite corresponds with much higher or lower temperatures in the pseudosection and most likely reflects the change in composition during the S2 lower temperature overprint. The measured Si content in white mica [Si (a.p.f.u.) = 3.045–3.95] corresponds to the *P–T* conditions determined by the garnet composition (Fig. 6a). This suggests that white mica may have been a stable phase of the S1 assemblage close to the S1 peak. In conclusion, the subvertical S1

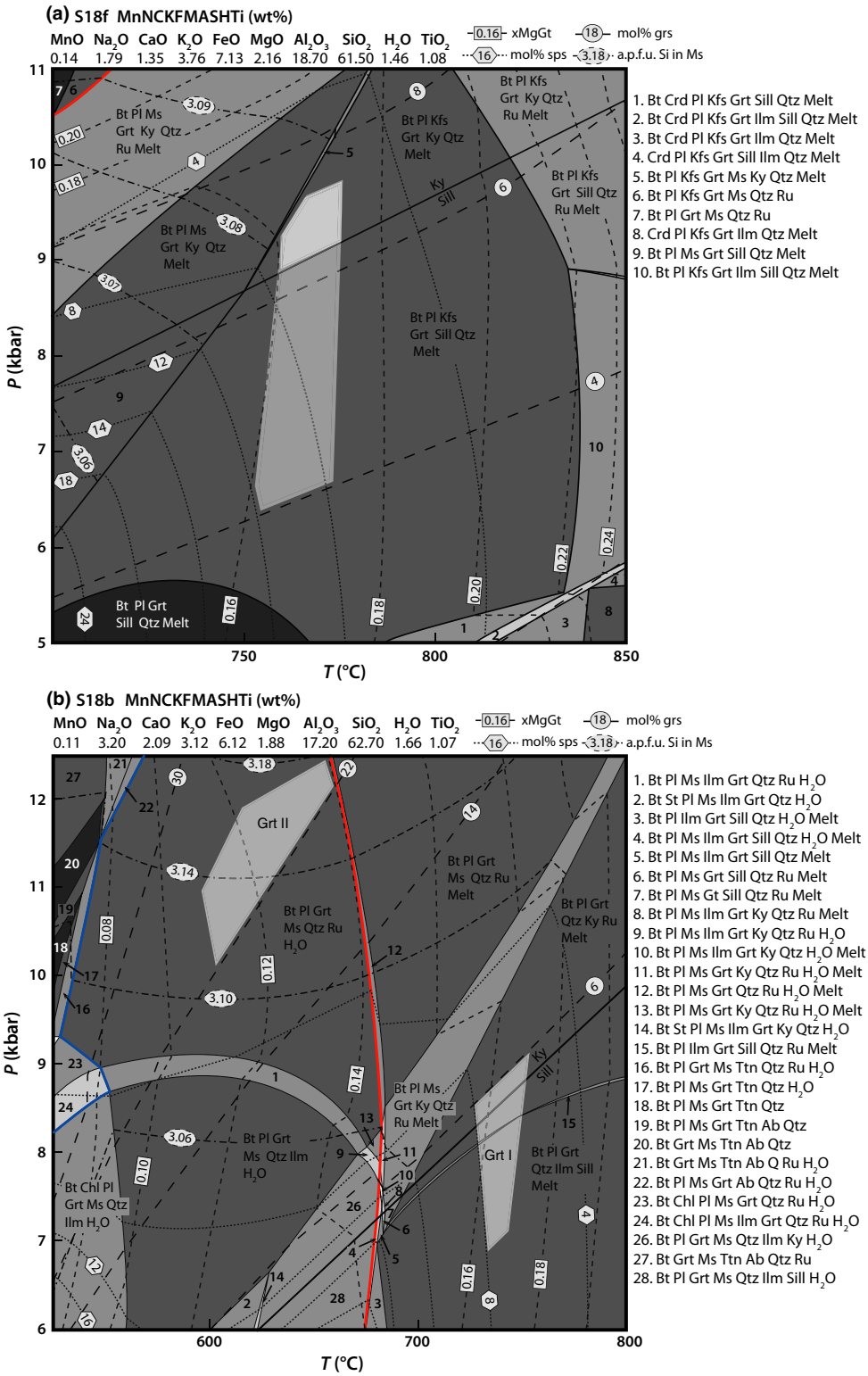

Fig. 6. Results of phase equilibrium modelling in the MnNCKFMASHTi system. (a) Pseudosection contoured for X_{Mg}, and mol.% of grossular and spessartine components showing modelling results for sample S18f collected from S1. The red line shows the melt-in reaction. Resulting *P–T* estimates are defined by the light grey and dark grey boxes (see text for explanation). (b) Pseudosection contoured for X_{Mg}, and mol.% of grossular and spessartine components showing modelling results for sample S18b collected from S2. The red and blue lines show the melt-in and titanite-in reactions respectively. The grey boxes show resulting *P–T* estimates for metamorphic events associated with formation of S1 (core Grt I composition) and S2 (rim Grt II composition). Bulk rock compositions used for the two pseudosections are also indicated in the figure.

fabric is interpreted to have formed at 750–775 °C and 6.3–9.8 kbar, with peak conditions at 760–775 °C and ~8.8–9.8 kbar (Fig. 6a).

Sample S18b is clearly polymetamorphic and shows remnants of the S1 assemblage overprinted by the younger S2 assemblage (Figs 2a & 5a–c). Although the S2 assemblage of GrtII–Bt–Ms–Plg–Qtz is dominant, the refractory garnet I in this sample preserves its original composition (Fig. 4b,c). Therefore, the distinct core garnet I and rim garnet II compositions in this sample (Fig. 4b,c) can be used to estimate *P–T* conditions of both S1- and S2-forming events (Fig. 6b). The composition of garnet I (Fig. 4b,c; Table S1; prp 15–17 mol.%, sps 2–5 mol.%, grs 4–6 mol.%) plots above the solidus into the stability fields of Bt–Plg–Grt–Qtz–Ky/Sil-Ru/Ilm (Grt I grey box in Fig. 6b). This is consistent with the presence of sillimanite inclusions in the garnet cores (Fig. 5c) at ~740 °C and ~6.8–8.5 kbar in the stability field of sillimanite. However, the frequent occurrence of kyanite in the subvertical fabric sampled just few metres away suggests that S18b had also been in the higher pressure kyanite stability field, which is in agreement with the observation of rutile in the S1 fabric, shown to be stable towards higher pressure (Figs 3f & 6b). The Ti content in the biotite inclusion in garnet I is also consistent with this proposed *P–T* range. Thus, the resulting *P–T* conditions for S1 in sample S18b are estimated at ~730–750 °C and ~7–9 kbar, with peak conditions in the kyanite stability field at ~8.2–9 kbar, consistent with the results from sample S18f.

The composition of garnet II can be used to estimate initial conditions during formation of the S2 fabric (Fig. 6b). The garnet II composition with X_{Mg} 0.11–0.14, grs 22–26 mol.% and sps 2–3 mol.% (Fig. 4c; Table S1) plots into the stability field of Bt–Plg–Grt–Ms–Qtz–Ru (Fig. 6b). Based on these garnet II isopleths, the *P–T* estimates for the initial formation of the subhorizontal fabric are constrained to ~600–660 °C at ~10–12.5 kbar.

The Ti and X_{Mg} in biotite as well as the An component of plagioclase in the matrix of this sample (Table S2) are in good agreement with the inferred *P–T* range in the pseudosection. The white mica, which defines the S2 fabric in both samples S18b and S18d, has a phengitic composition but its measured silica values plot below or in the lower half of the pressure range defined by the garnet II composition (Table S2; 3.08–3.14 a.p.f.u.; ~9–11 kbar, Fig. 6b). This growth of white mica at pressures lower than the S2 peak could suggest: (i) late S1 white mica equilibrated during evolution from S1 to S2 (as suggested by the presence of late white mica in S1 samples with a silica content plotting between the two events; Fig. 6a) or (ii) white mica growth continued after the S2-forming event, during retrograde metamorphism. Given the presence of titanite rims on rutile grains in the S2 fabric (Fig. 5d), which is consistent with a post-S2 retrograde path, both options for white mica growth are possible. A decrease in temperature of 50–60 °C from the S2 peak introduces titanite below ~550 °C (blue line in Fig. 6b), and given the lack of albite in the S2 assemblage and the Si content of white mica indicating lower pressure, this decrease in temperature was likely concurrent with at least a small decrease in pressure (i.e. stability fields 16–18 in Fig. 6b).

Zirconium-in-rutile thermometry

Rutile is abundant in the S1 fabric, where it occurs as small crystals 50–150 μm in length elongated parallel to S1, suggesting that it is part of the peak metamorphic assemblage (Fig. 3f). In samples of the S2 fabric, rutile is present as small grains surrounded by ilmenite and/or titanite (Fig. 5d). According to the phase equilibrium modelling, rutile was stable both during the formation of S1 and the initial stages of S2 formation, with titanite becoming stable during cooling (Fig. 6).

In order to constrain rutile crystallization and/or cooling temperatures and to compare them with the temperatures obtained from phase equilibrium modelling, Zr-in-rutile thermometry was applied (e.g. Zack *et al.*, 2004; Ferry & Watson, 2007; Tomkins *et al.*, 2007) using the Zr-in-rutile calibration of Tomkins *et al.* (2007) for the β-quartz field. For the thermometry on the S1 and S2 fabrics, the respective pressures of 8 and 11 kbar obtained from the phase equilibrium modelling (Fig. 6) were used. Fifty-two analyses were conducted on 29 rutile grains from sample Sk3d (S1). The detection limit for Zr was 55–60 ppm, and the analytical uncertainty (2σ) was 11–34% over the range of measured Zr values (±30–33 ppm). Three analyses were discarded due to a Si content of >1000 ppm, which is probably the result of microscopic zircon inclusions. The measured Zr content varies from 92 to 269 ppm, with most analyses between 100 and 210 ppm (Table S3). The temperature estimates vary from 550 + 18 °C/−26 °C to 630 + 9 °C/−10 °C (Table S3, only electron microprobe analytical errors considered). These estimates are considerably lower than the peak temperature estimate for S1 obtained by phase equilibrium modelling (Fig. 6). Fourteen analyses were conducted on three rutile grains from sample Sk3a (S2). The Zr content varies from 100 to 320 ppm (Table S3). Temperature estimates for these values vary from 580 + 20 °C/−25 °C to 660 ± 8 °C (Table S3), which is within error or slightly lower compared to the peak temperature for S2 obtained by phase equilibrium modelling (Fig. 6b).

GEOCHRONOLOGY

U–Pb LA-ICP-MS dating of detrital zircon

In order to derive a maximum depositional age for the Eidet metasedimentary sequence, and to com-

pare the detrital zircon age spectra with those used to define the Sværholt and Sørøy successions, 152 U–Pb LA-ICP-MS analyses on 151 grains from sample Sk3a (Fig. 7a; Table S4) were undertaken. Sixty-one analyses show >5% central discordance and are therefore excluded from the age probability plot (Fig. 7b). From the remaining 91 analyses, 34 scatter between 1830 and 1280 Ma, whereas 55 fall into the main age group 1200–900 Ma, with a peak of *c*. 1030 Ma (Fig. 7b). The three youngest grains within this main age group have a weighted average age of 937 ± 14 Ma (MSWD = 0.87), which we interpret as a conservative maximum depositional age for this sample (Table S4). The remaining two analyses give $^{207}Pb/^{206}Pb$ ages of 839 ± 13 and 761 ± 12 Ma. The younger analysis plots slightly off the Concordia curve and comes from a spot that overlaps two different cathodoluminescence (CL)-zones, indicating that it could represent a mixed age. The older analysis is within error of a well-known magmatic event recorded elsewhere in the KNC, and given the fact that the sample experienced at least two metamorphic events up to partial melting after deposition (S1 and S2), we interpret this analysis as representing metamorphic zircon growth or diffusional Pb loss.

U–Pb SIMS dating of zircon from the S1-parallel leucosome

To determine the timing of partial melting and the formation of the S1 fabric, zircon from an S1-parallel leucosome was dated by SIMS (sample Sk3c). Zircon from this sample forms euhedral, short-prismatic crystals with a length of 100–250 μm. The grains have a very low CL emission, and are mostly unzoned (Fig. 8a). In the CL, a few grains show bright, ~20 μm wide cores, partly with sharp boundaries, partly with a blurry transition into the surrounding rims (Fig. 8a). Forty spots were analysed on 38 grains, with 12 analyses targeting the CL-bright cores. The cores have Th/U values of >0.1, except for three analyses with Th/U < 0.1 (Table S5). Five analyses are discordant, possibly representing mixing between the small CL-bright cores and the surrounding rims. The remaining seven core analyses plot on Concordia and give $^{207}Pb/^{206}Pb$ ages between 768 ± 45 and 1028 ± 13 Ma (Table S5; Fig. 8b). Twenty-eight analyses come from CL-dark, unzoned grains. They all have Th/U values of <0.04 and U contents of up to 2325 ppm and plot close to or on Concordia. One analysis is clearly younger (and has a large error in the $^{207}Pb/^{206}Pb$ age) and one analysis is clearly older than the main cluster (Fig. 8b). Many of the 26 analyses from the main cluster plot slightly on the reverse side of Concordia (Fig. 8b). This is a common feature of SIMS data obtained from high-U zircon, reflecting the different sputtering behaviour of metamict zircon compared to the lower U reference

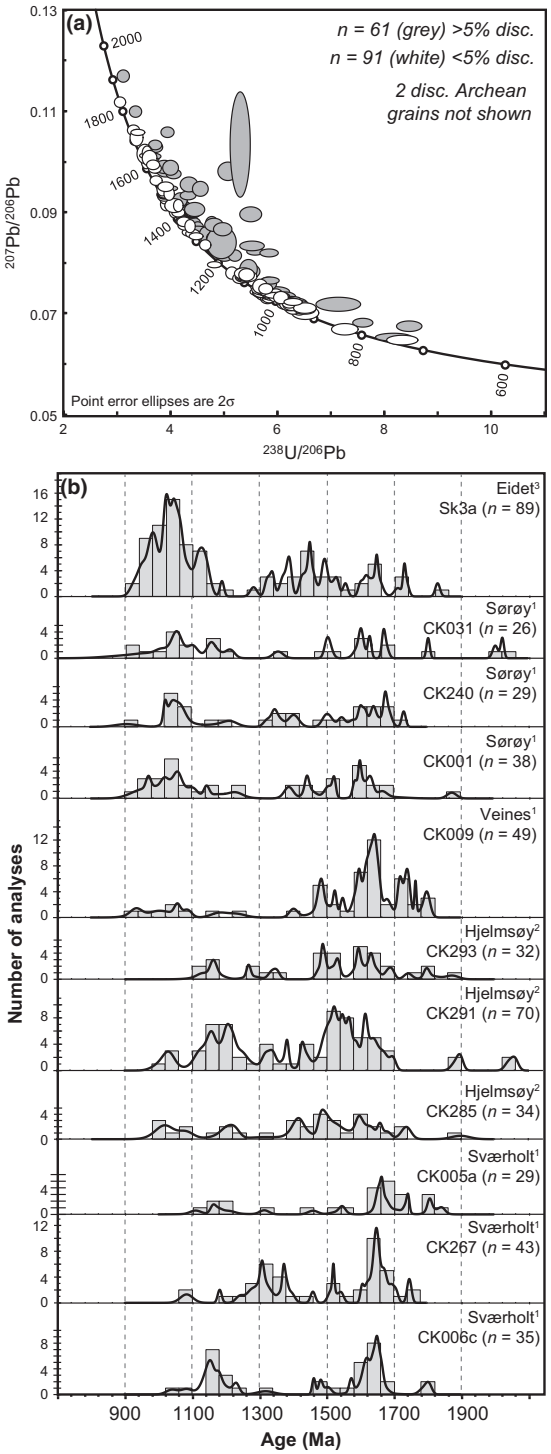

Fig. 7. Detrital zircon results from sample Sk3a. (a) Tera-Wasserburg diagram showing all 152 LA-ICP-MS analyses. (b) Probability plots and frequency histograms (analyses <5% discordant) of all available detrital zircon samples from the KNC ($^{207}Pb/^{206}Pb$ ages used). (1) Kirkland *et al*. (2007b), (2) Kirkland *et al*. (2008b), (3) This study. Note that sample CK005a also contains a small Archean (2700–2900 Ma) population of four grains not shown in the plot.

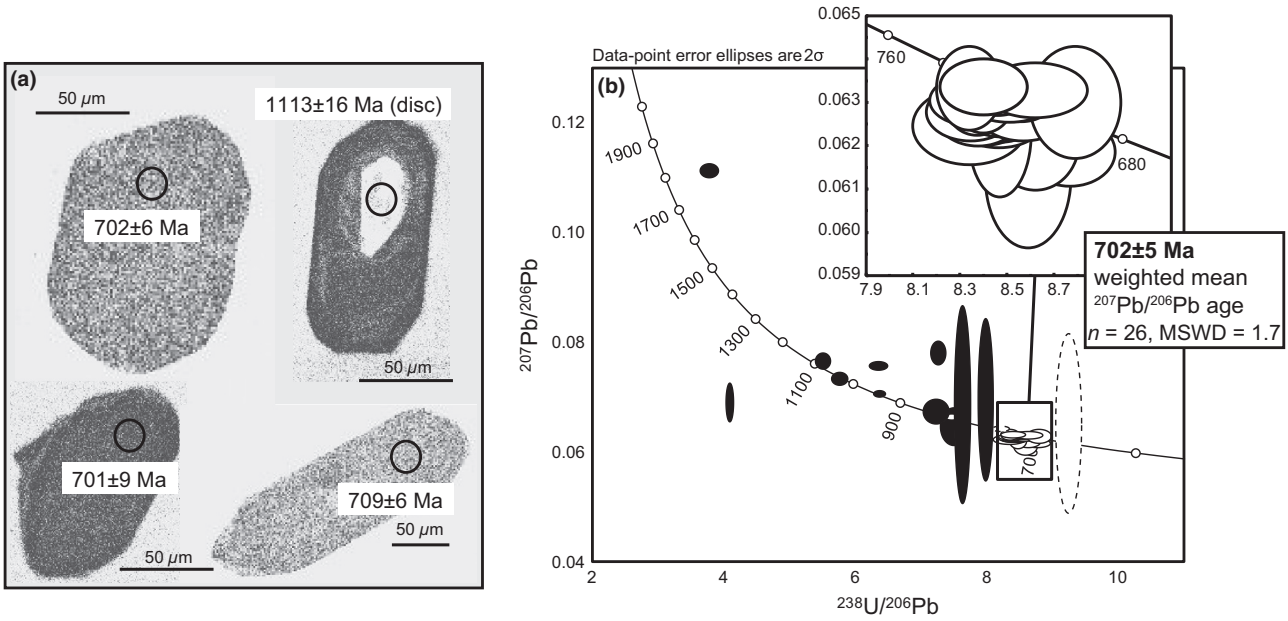

Fig. 8. (a) CL images of zircon grains from the leucosome sample Sk3c. Approximate SIMS spot locations are indicated, and their $^{207}Pb/^{206}Pb$ ages are given. (b) Tera-Wasserburg diagram for SIMS zircon analyses from the leucosome sample Sk3c.

zircon, and we therefore consider the $^{207}Pb/^{206}Pb$ ages to be more reliable than the $^{238}U/^{206}Pb$ ages. The weighted average $^{207}Pb/^{206}Pb$ age of all 26 analyses is 702 ± 5 Ma (MWSD = 1.7), which we interpret to best represent the crystallization age of the leucosome.

U–Pb SIMS dating of monazite from the S1-parallel leucosome and melanosome

In order to better understand the nature and metamorphic conditions of the S1 event, the occurrence and age of monazite in both leucosome (sample Sk3c) and melanosome (sample Sk3d) were studied. In the leucosome, six monazite grains were observed in thin section, all located at grain boundaries of quartz, plagioclase, biotite and garnet. The mineral separate yielded >50 grains ~50–150 μm in diameter. They are light greenish-yellowish, subhedral, rounded to angular grains. High-contrast BSE images show no zoning, or very subtle zoning, in these grains, and EMPA analyses of 13 grains show that they have a very homogeneous composition (Table S6; Fig. 9a). Ten SIMS analyses were conducted on 10 different grains. All analyses are concordant and $^{207}Pb/^{206}Pb$ dates range from 710 ± 9 to 609 ± 12 Ma (Table S7; Fig. 9a). The seven oldest dates form a cluster with Concordia age of 698 ± 11 Ma (Fig. 9a), which falls within error of the zircon age obtained from the same leucosome sample (Fig. 8). Three analyses are younger than this main cluster, and scatter along Concordia (Fig. 9a).

In the melanosome (sample Sk3d), ~40 monazite grains were observed in thin section, occurring at grain boundaries in contact with quartz, plagioclase, biotite, muscovite, garnet or sillimanite or as inclusions within biotite, plagioclase or quartz. The mineral separate yielded >70 grains ~50–150 μm in diameter. They are light yellowish, subhedral, rounded to angular grains. Most grains show no zoning in high-contrast BSE images; however, four grains show subtle irregular zoning. Twelve EMPA analyses of unzoned grains show that they have a very homogeneous chemical composition, comparable to the monazite compositions from the leucosome (Table S6; Fig. 9b). Two of the four zoned grains show core compositions similar to the unzoned grains, whereas the other two zoned grains have cores with higher ThO_2 and lower Y_2O_3 values (Table S6; Fig. 9b). Three of the four zoned grains have rims with similar composition to the main group of the unzoned grains, whereas one of the grains has a rim with less ThO_2 but more REE (Table S6). Twenty SIMS analyses were conducted on 16 grains. All analyses plot on Concordia at 2σ and $^{207}Pb/^{206}Pb$ dates range from 786 ± 12 to 594 ± 18 Ma (Table S7; Fig. 9b). The oldest analysis comes from the Th-rich core of grain 12 (Table S7; Fig. 9b). The rim of this grain belongs to an array of 14 analyses spread along Concordia from *c.* 780 to 700 Ma, with dates older than, and overlapping with, the main cluster of monazite dates from the leucosome sample Sk3c (Fig. 9). From the remaining analyses, one is slightly discordant (core of grain 37,

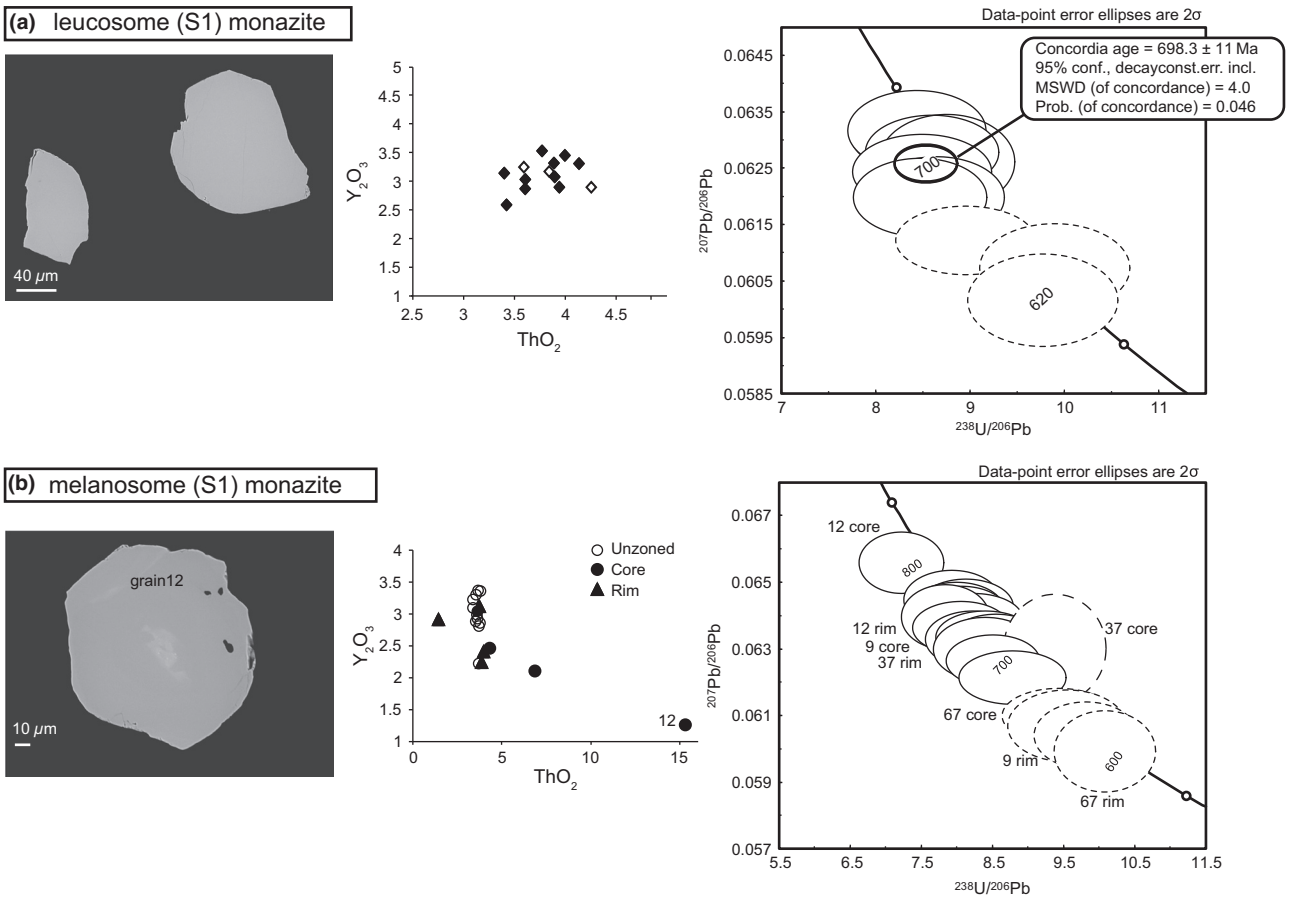

Fig. 9. (a) High-contrast BSE image, ThO_2 *v.* Y_2O_3 compositional diagram and Tera-Wasserburg diagram for monazites from the leucosome sample Sk3c. The white rectangles in the compositional diagram correspond to the stippled analyses in the Tera-Wasserburg diagram. (b) High-contrast BSE image, ThO_2 *v.* Y_2O_3 compositional diagram and Tera-Wasserburg diagram for monazite from melanosome sample Sk3d.

Fig. 9b), whereas the youngest four analyses scatter along Concordia from *c.* 680 to 580 Ma, among them the core and rim analyses from grain 67 (Fig. 9b).

U–Pb TIMS dating of metamorphic rutile

To test the potential of the observed rutile (Figs 3f & 5d) as a geochronometer, and to compare these results with the U–Pb dates from zircon, monazite and titanite, 14 rutile grains from the leucosome (Sk3c), the melanosome (Sk3d) and the S2 fabric (Sk3a) were analysed by TIMS. One analysis from Sk3c and one analysis from Sk3a contain too little U (<0.3 ppm) to calculate a meaningful U–Pb date (Table S8). The remaining analysis from Sk3c plots on Concordia with a $^{238}U/^{206}Pb$ age of 438 ± 3 Ma (Fig. 10a, grey ellipse). Of the seven analyses from Sk3d, three analyses plot on Concordia (Fig. 10a, white ellipses). Two of the three analyses overlap with $^{206}Pb/^{238}U$ ages of 433 ± 2 and 432 ± 4 Ma (Table S8; Fig. 10a). The third analysis is clearly younger with a $^{206}Pb/^{238}U$ age of 419 ± 1 Ma (Table S8; Fig. 10a). The remaining four analyses are reversely discordant, possibly due to an unrecognized interference on ^{204}Pb; their $^{206}Pb/^{238}U$ ages range from 430 ± 2 to 419 ± 7 Ma (Fig. 10a). The four analyses from Sk3a scatter along Concordia with $^{206}Pb/^{238}U$ dates between 552 ± 16 and 440 ± 3 Ma (Table S8; Fig. 10a, dashed ellipses). The oldest of these is a black rutile grain, which probably contains over/intergrowths of ilmenite.

U–Pb TIMS dating of metamorphic titanite

Titanite crystals of ~100–500 μm length elongated parallel to S2 are very abundant in samples from the S2 fabric (Fig. 5d). Some of this titanite overgrew or replaced rutile and/or ilmenite (Fig. 5d). Titanite was separated from sample Sk3a and only clear grains without inclusions were selected. Only one type of titanite grain was observed in the mineral separate. Nine single- to multigrain fractions (Table S8; Fig. 10b) were analysed. Two analyses have large

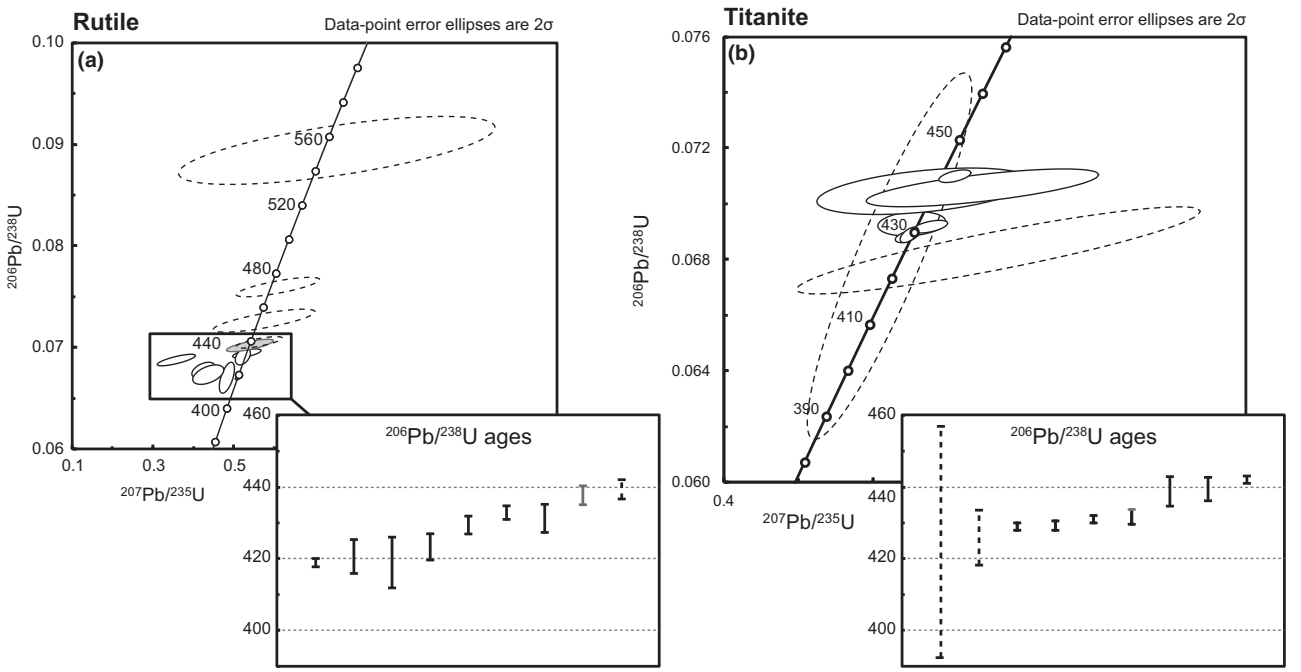

Fig. 10. (a) Concordia diagram for U–Pb TIMS rutile analyses. Grey ellipse: leucosome sample Sk3c; white ellipses: melanosome sample Sk3d; dashed ellipses: S2 fabric sample Sk3a. (b) Concordia diagram for U–Pb TIMS titanite analyses from sample Sk3a.

errors in their $^{206}Pb/^{238}U$ as well as $^{207}Pb/^{235}U$ ratios (Table S8; Fig. 10b). The remaining seven analyses scatter along Concordia with $^{238}U/^{206}Pb$ ages that range from 442 ± 1 to 429 ± 1 Ma (Fig. 10b).

DISCUSSION

Deposition of the Eidet rocks as a part of the Sørøy succession

Within the northeastern part of the KNC, Kirkland *et al.* (2007b, 2008b) defined two different sedimentary successions, the Sværholt and Sørøy successions, based on detrital zircon age patterns and tectonometamorphic evolution (Fig. 1). The Sværholt succession shows a maximum depositional age of 1030 ± 16 Ma, and is cut by *c.* 980–960 Ma granitic intrusions. In contrast, the Sørøy succession shows a maximum depositional age of 910 ± 15 Ma, and distinct tectonometamorphic events at *c.* 850–820 Ma, *c.* 710–680 Ma, *c.* 600 Ma and *c.* 580–520 Ma (Kirkland *et al.*, 2006a, 2007b; Corfu *et al.*, 2007). Sample Sk3a shows a maximum depositional age of 937 ± 14 Ma, similar to the maximum depositional age of the Sørøy succession (Figs 7 & 11a). In addition, there is clear evidence for a high-*T* metamorphic event at *c.* 710–680 Ma in the Eidet rocks, which is also common in the Sørøy succession. The *c.* 980–960 Ma plutons typical for the Sværholt succession have not been discovered in the Eidet region so far. The two isolated zircon dates at 839 ± 13 and 761 ± 12 Ma in sample Sk3a could be the result of the protracted Neoproterozoic evolution of the Sørøy succession, reflecting a first stage of metamorphic growth during the 850–820 Ma events and/or mixing with 700 Ma metamorphic rims. The detrital age spectrum from Sk3a shows similarities with the patterns from the Sørøy succession (Fig. 7b) and is statistically not different from the three available Sørøy spectra ($P > 0.05$ in K–S test). Therefore, in the absence of a better stratigraphic control, we correlate the Eidet metasedimentary rocks with the Sørøy succession of Kirkland *et al.* (2007b, 2008b).

Partial melting of the Eidet rocks: interpretation of U–Pb zircon ages

The first tectono-metamorphic event recognized in the Eidet locality is represented by the S1 fabric, which formed at 730–775 °C and 6.3–9.8 kbar, above the wet solidus, overlapping the sillimanite and kyanite stability fields (Figs 6 & 11b). The high-U zircon from the leucosome reveal a crystallization age of 702 ± 5 Ma (Figs 8 & 11a), indicating that peak metamorphic conditions had been reached at this time and crystallization of melt started. This age is within error of the intrusion age of the nearby Sandøra granitic gneiss on Skjervøy (Fig. 1; 706 ± 3 Ma, Corfu *et al.*, 2007), as well as a leucosome age from the Eidvågeid paragneiss farther northwest (Fig. 1; 709 ± 4 Ma, Kirkland *et al.*, 2006a). These ages indicate that Neoproterozoic

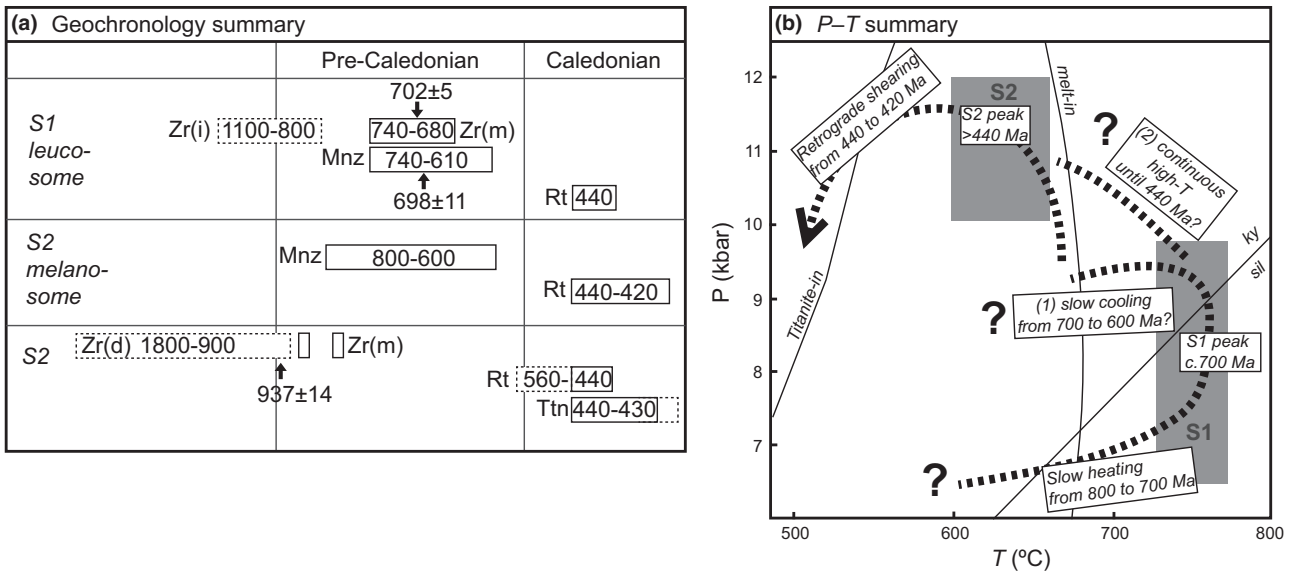

Fig. 11. (a) Summary table showing all geochronology results. Abbreviations: (i) inherited, (m) metamorphic, (d) detrital. (b) Summary *P–T* diagram. Our data set does not allow the unambiguous locations of the Eidet rocks during the time span from 700 to 440 Ma. Either the rocks cooled slowly below the solidus after the S1 peak until 600 Ma (monazite, interpretation 1), or they stayed at high temperatures after the S1 peak (with partial resetting of monazite ages, interpretation 2) until cooling and compression occurred at the onset of Caledonian deformation at *c*. 440 Ma.

metamorphism, partial melting and deformation have affected the Sørøy succession of the KNC for at least 100 km along strike (Fig. 1).

Long-lasting Neoproterozoic metamorphism: interpretation of U–Pb monazite ages

The U–Pb monazite dates from the S1 fabric are more difficult to interpret. The main monazite age cluster from the leucosome (698 ± 11 Ma, Figs 9a & 11a) overlaps with the age obtained from zircon in the same leucosome (Fig. 8b), suggesting that most monazite formed during crystallization of the melt at *c*. 710–700 Ma, at or shortly after the metamorphic peak. The U–Pb monazite dates from the melanosome sample, however, spread strongly along Concordia, covering a time span of nearly 200 Ma between 800 and 600 Ma (Figs 9b & 11a). Most monazite grains have a homogeneous composition similar to the grains from the leucosome. The few grains with a core–rim relationship generally are older in the core and younger in the rim, but these ages do not correspond to any specific population, neither in terms of age nor of composition (Fig. 9b).

A similar spread of concordant monazite dates has been documented elsewhere in the Sørøy succession, where monazite single-grain U–Pb TIMS dates scatter from *c*. 810 to 640 Ma (Corfu *et al*., 2007; Roberts, 2007). Thus, the spread in monazite dates is a reproducible feature in the metapelitic rocks of the Sørøy succession, obtained with both SIMS and TIMS methods. Corfu *et al*. (2007) speculated that the single monazite crystals analysed by TIMS may represent composite grains consisting of different generations, resulting in meaningless apparent ages. However, our BSE, EMP and SIMS analyses exclude the possibility of having analysed composite age zones, indicating that each date is representative of the particular analysed zone (Tables S6 & S7; Fig. 9). We envisage two possible ways of interpreting the scatter of these metamorphic monazite dates.

Interpretation 1

The monazite dates represent the true formation age of each grain, and protracted mineral growth has caused the observed age spread. In metapelitic rocks, growth of metamorphic monazite can occur during prograde metamorphism above ~500–600 °C (e.g. Smith & Barreiro, 1990; Rubatto *et al*., 2001, 2006; Wing *et al*., 2003; Kohn *et al*., 2005; Janots *et al*., 2008; Spear, 2010; Gasser *et al*., 2012). Hence, the array of 15 monazite dates scattering from *c*. 800 to 700 Ma may represent continuous monazite growth during slow prograde metamorphism from ~500 to ~775 °C with a heating rate of ~3 °C Ma^{-1}. Post-peak crystallization of monazite during initial cooling across the solidus (often coupled with garnet consumption) has been documented by many workers (e.g. Foster & Parrish, 2003; Pyle & Spear, 2003; Foster *et al*., 2004; Kohn *et al*., 2005), and therefore monazite dates that are younger than the metamorphic peak at 700 Ma could also fit into a model of protracted monazite growth. In our samples, the youngest monazite dates could therefore indicate the time when the migmatite cooled below the solidus at

~680 °C (Fig. 6), implying a relatively slow cooling rate of ~1 °C Ma^{-1} from *c.* 700 to 600 Ma (Fig. 11b, interpretation 1). However, in contrast to other studies which have demonstrated monazite growth at different points during pro- and retrograde *P–T* paths (e.g. Foster & Parrish, 2003; Foster *et al.*, 2004; Gibson *et al.*, 2004; Kohn *et al.*, 2005), our monazite shows surprisingly little variation in composition, suggesting that mechanisms other than protracted growth could potentially have caused the large age spread.

Interpretation 2

All monazite grains originally crystallized at the same time, and secondary diffusion may have partially reset the ages at one or different times. In principle, amphibolite facies monazite as old as 850 Ma could have been present in the Sørøy succession (e.g. Daly *et al.*, 1991; Kirkland *et al.*, 2006a, 2008b), and such a population of 850 Ma monazite could have been exposed to diffusional modification during subsequent high-*T* events at *c.* 710–700 Ma (730–775 °C, this study) and/or at *c.* 580–560 Ma (SIP, 760–820 °C; Menegon *et al.*, 2011). This in turn could lead to a sub-concordant array of analyses scattering between the original and the overprinting events (Fig. 9b). It has been suggested that monazite grains of 50–200 μm in size can lose significant amounts of Pb if they remained for more than 10 Ma at temperatures above ~600–700 °C (e.g. Copeland *et al.*, 1988; Parrish, 1990; Suzuki *et al.*, 1994; Smith & Giletti, 1997). However, more recent results suggest that diffusional loss of Pb might be negligible for most natural monazite (e.g. Bingen & van Breemen, 1998; Zhu & O'Nions, 1999; Seydoux-Guillaume *et al.*, 2002; Foster & Parrish, 2003; Cherniak *et al.*, 2004; Gardes *et al.*, 2006; Cherniak, 2010). Therefore, some diffusional rejuvenation of older monazite dates would only be possible if they had remained at elevated temperatures of ~600–700 °C for most of the time between the distinct events at 850–820 Ma, 710–680 Ma, 580–560 Ma and possibly 440–420 Ma (Fig. 11b, interpretation 2). Fluid-assisted dissolution/re-precipitation mechanisms might also alter both composition and age of monazite (e.g. Teufel & Heinrich, 1997; Seydoux-Guillaume *et al.*, 2002; Harlov *et al.*, 2011; Williams *et al.*, 2011). However, these mechanisms usually lead to compositional zoning and specific microstructures that can be clearly identified by EMP/BSE analyses. No such zonations and microstructures were observed, ruling out the possibility for significant fluid-assisted alteration of the grains.

In our opinion, it is currently not possible to distinguish unambiguously between the protracted growth and the diffusional resetting interpretations. However, both interpretations require that the Eidet rocks experienced temperatures of at least 600 °C for at least the time between *c.* 800 and 600 Ma, indicating lower crustal conditions for this entire time span.

Interestingly, monazite is absent in samples of the S2 fabric, and most of the REE seem to be hosted in allanite/epidote grains (Table 1), indicating that monazite was no longer stable during S2 at 600–660 °C and 10–12 kbar. This inference is in agreement with petrological modelling of monazite and allanite/epidote stability in metapelitic rocks of similar composition, which shows that monazite is replaced by epidote/allanite when cooling below ~700 °C at 10 kbar (Janots *et al.*, 2007). Therefore, in our case, monazite is not a suitable geochronometer for identifying the age of the S2 fabric.

Diffusional resetting of rutile during S2: interpretation of Zr-in-rutile thermometry and U–Pb rutile ages

Based on microstructures and phase equilibrium modelling, rutile represents a stable part of the S1 assemblage formed at 730–775 °C and 6.3–9.8 kbar (Figs 3f & 6). The Zr-in-rutile thermometer is commonly considered to be a robust thermometer at high-*T* conditions up to granulite facies (e.g. Zack *et al.*, 2004; Luvizotto & Zack, 2009; Kooijman *et al.*, 2012; Ewing *et al.*, 2013). However, the temperature range of 550–630 °C calculated by using this thermometer for the S1 (Fig. 3f) is considerably lower than the S1 peak temperatures of 730–775 °C estimated from phase equilibrium modelling (Table S3; Fig. 6). Instead, these temperatures are similar to those obtained for the S2 fabric from both Zr-in-rutile thermometry and phase equilibrium modelling (600–660 °C, Table S3, Fig. 6). We therefore suggest that the Zr-in-rutile temperatures from all analysed grains most likely represent temperatures attained during the formation of the S2 fabric. Interestingly, the lowest temperatures recorded by the rutile (~550 °C) roughly correspond to the point where rutile is replaced by titanite in the pseudosection (Fig. 6b). Re-equilibration of mineral compositions in the S1 fabric during the S2-forming event is also documented from biotite (X_{Mg} of biotite in the calculated pseudosection for the S1 fabric indicates lower than peak temperatures), and from garnet (transition zones between garnet I and II in S1, Fig. 4a).

According to experimental diffusion data for Zr in rutile, small rutile grains (50–100 μm) can lose their Zr when heated above 650 °C for longer than *c.* 1 Ma (fig. 6 in Cherniak *et al.*, 2007). Hence, if the S2-forming event lasted for longer than *c.* 1 Ma, this would have been sufficient to re-equilibrate the Zr of the small rutile grains in both fabrics. In addition, based on modelling of natural Zr diffusion profiles in rutile, it has been postulated that increased pressure and the presence of aqueous fluids might further enhance diffusion of Zr in rutile (Lucassen *et al.*, 2010). Both requirements are satisfied in our case as the S2 fabric formed at elevated pressures of

10–12 kbar and in the presence of aqueous fluids, inferred from the increased quantity of white mica in the S2 samples. Similar natural cases of diffusional resetting of Zr-in-rutile have been previously reported at temperatures of ~600–750 °C (e.g. Watson *et al.*, 2006; Luvizotto & Zack, 2009; Jiao *et al.*, 2011; Meyer *et al.*, 2011). We therefore interpret the calculated Zr-in-rutile temperatures to result from diffusion reset of rutile during the S2-forming event.

The U–Pb dates of rutile from both fabrics are significantly younger than the age of the S1 fabric derived from zircon and monazite (Figs 10 & 11a). This again indicates that similar to the Zr-in-rutile signature discussed above, the U–Pb signature of the rutile in the S1 fabric does not reflect timing of its crystallization during the S1-forming event. In contrast, the U–Pb dates of the rutile overlap with those from titanite (Figs 10 & 11a), which clearly grew during the S2-forming event (Fig. 5d). Both experimental data and studies of natural rutile show considerable Pb diffusion in rutile above ~600–650 °C and in some cases even above ~380–490 °C (e.g. Mezger *et al.*, 1989; Cherniak, 2000; Li *et al.*, 2003, 2011; Vry & Baker, 2006; Kooijman *et al.*, 2010; Warren *et al.*, 2012). Given these results and assuming that the S2 overprint spanned at least several million years at elevated temperatures of 600–660 °C, resetting of the U–Pb system by diffusion in all analysed rutile grains from the S1 fabric is likely, and we therefore interpret our U–Pb rutile dates as representing cooling ages.

Interestingly, the U–Pb dates of rutile from the S1 fabric are slightly younger than the U–Pb dates of rutile in the S2 fabric (Figs 10 & 11a). All rutile grains observed in thin sections in the S2 fabric are inter/overgrown by either ilmenite and/or titanite, whereas the grains in the S1 fabric are not (Figs 3f & 5d). At least one of the rutile grains from S2 analysed by TIMS might have contained ilmenite over/intergrowths (black colour of analysed grain, Table S8). According to the phase equilibrium modelling, ilmenite probably was stable during S1, whereas titanite clearly grew during S2 (Fig. 6). Both minerals may have shielded the U–Pb system of the rutile from diffusional resetting by physically overgrowing them, and the older analyses (up to 560 Ma, Figs 10 & 11a) may thus represent partially reset dates from originally even older grains.

Duration of S2 shearing: interpretation of U–Pb titanite ages

Based on microstructures and phase equilibrium modelling, titanite grew parallel to the S2 fabric at the expense of rutile at temperatures below ~550 °C (Figs 5d & 6b). U–Pb dates for the analysed titanite grains scatter from 440 to 430 Ma, with two analyses that have large errors scattering down to 420 Ma (Figs 10 & 11a). In order to interpret these titanite dates, it is again important to evaluate whether they represent growth or cooling ages. Both natural samples and experimental data on Pb diffusion in titanite indicate that below ~550–600 °C, Pb diffusion in titanite is very limited, and that even U–Pb signatures of high-T events up to 800 °C can be preserved (Mezger *et al.*, 1991; Cherniak, 1993; Frost *et al.*, 2000; Kylander-Clark *et al.*, 2008; Kohn & Corrie, 2011; Warren *et al.*, 2012). We therefore interpret the 440–430 Ma titanite dates as representing growth of titanite during S2 formation below ~550 °C. The U–Pb rutile dates interpreted as cooling ages are within error of the U–Pb titanite growth ages, indicating that in this particular case, the closure temperature for U–Pb in rutile overlaps with crystallization temperature for titanite at ~550 °C. Together, these ages indicate that S2 shearing occurred below ~550 °C for at least 10 Ma from *c.* 440–430 Ma, possibly continuing until *c.* 420 Ma.

Tectonic implications for the evolution of the KNC

The Neoproterozoic evolution

The geodynamic setting and significance of the Neoproterozoic tectono-metamorphic/magmatic events, which are becoming more widely documented from the Sørøy succession in the upper Kalak nappes (Daly *et al.*, 1991; Kirkland *et al.*, 2006a, 2007b, 2008b; Corfu *et al.*, 2007, 2011; this study), is open to debate. Two contrasting interpretations have been suggested. (i) They could represent mainly rift-related deformation and magmatism due to the break-up of Rodinia along the extending Baltoscandian margin (e.g. Paulsson & Andreasson, 2002; Roberts, 2003; Siedlecka *et al.*, 2004). This model, however, is difficult to reconcile with the compressional and thrust-related Neoproterozoic structures documented by Kirkland *et al.* (2006a, 2007b). (ii) Alternatively, the Neoproterozoic events could indicate successor basin development and accretionary tectonics along an earlier, pre-Caledonian active continental margin (e.g. Kirkland *et al.*, 2006a, 2007b; Corfu *et al.*, 2007, 2011).

In the rift model, it is assumed that the Sørøy succession was deposited on extending (Baltican) continental crust at *c.* 900 Ma, and that this continental extension and rifting continued until the onset of Iapetus drifting at *c.* 600 Ma. In such a setting, relatively high T/P ratios in the andalusite/sillimanite stability fields would be expected due to the thinning and heating of continental crust from below, as for example documented for the Permian extensional metamorphism in the Alpine realm (e.g. Jeřábek *et al.*, 2008; Schuster & Stüwe, 2008). However, the S1 event is characterized by P–T conditions in the kyanite stability field, up to 9.8 kbar and 775 °C (Fig. 11b), indicating a low T/P ratio, atypical for extensional settings. Thus, it is unlikely that the

deposition of the Sørøy succession and the subsequent S1 metamorphism is the result of pre-Iapetus rifting. The low T/P ratio and the protracted period of nearly 200 Ma (from at least *c.* 800–600 Ma) at high P–T conditions indicated by the monazite ages is in better agreement with a collisional or active margin tectonic setting. Indeed, restoring the Caledonian southeast-directed thrusting of the KNC back to the northwest, the nappes align with the Timanian margin of Baltica, which experienced Neoproterozoic to Cambrian deformation, magmatism and metamorphism (e.g. Roberts & Siedlecka, 2002; Siedlecka *et al.*, 2004). Clearly, more work is needed to understand the geodynamic significance of Neoproterozoic tectono-metamorphic events recorded in the upper Kalak nappes, and in which paleogeographic setting they might have occurred.

The Caledonian evolution

The Caledonian evolution is clearly represented at the Eidet locality by the S2 event at 600–660 °C and 10–12 kbar (Figs 6b & 11b). Similar temperatures and pressures (650–700 °C and 8–10 kbar) are recorded by the rocks in the Øksfjord region during the last M3 event (Elvevold *et al.*, 1994), which most likely corresponds to the Caledonian metamorphism in the Eidet rocks. Interestingly, this Caledonian overprint has occurred at higher pressures than the pre-Caledonian partial melting event, indicating crustal thickening at the onset of this orogeny. The documented Caledonian deformation and metamorphism might have been facilitated by the infiltration of aqueous fluids, indicated by (i) the ubiquitous presence of white mica and the higher H_2O content of most of the samples from the Caledonian fabric at the Eidet locality and (ii) several pulses of anatectic melts in the Hjelmsøy shear zone (Kirkland *et al.*, 2009). Pre-Caledonian mineral assemblages, rock fabrics and ages are only preserved locally in lenses, due to the relative absence of retrograde reactions and deformation. Interestingly, the overprinting of rutile ages is more pronounced in the pre-Caledonian fabric S1 compared to the Caledonian fabric S2. The interpretation that this situation arises due to better barriers to diffusion/reaction represented by overgrowing ilmenite/titanite demonstrates the importance of such overgrowths for the preservation of relict assemblages and fabrics.

The subhorizontal S2 foliation and top-to-the-SE-shear senses are developed throughout the KNC, representing pervasive Caledonian thrusting, which has emplaced the KNC onto Baltica. The U–Pb titanite ages from the Eidet rocks constrain the age of retrograde Caledonian shearing (below ~550 °C) to *c.* 440–420 Ma (Figs 10 & 11), implying that Caledonian peak metamorphic conditions must have occurred prior to *c.* 440 Ma at the Eidet locality. Caledonian ages of *c.* 450–425 Ma are known from both granitic bodies, pegmatites and metamorphic fabrics elsewhere in the KNC (Kirkland *et al.*, 2006b, 2007a,b, 2009; Corfu *et al.*, 2006, 2011), constraining the main phase of the Caledonian orogeny in the KNC to the latest Ordovician–Silurian. Deformation ages from the underlying and overlying tectonic units indicate that Caledonian deformation might be oldest (*c.* 500 Ma) at the bottom of the nappe stack in the Gaissa and Laksefjord Nappe Complexes (e.g. Rice & Frank, 2003; Sundvoll & Roberts, 2003; Kirkland *et al.*, 2008a), and becomes younger upwards (*c.* 430–420 Ma in the overlying Magerøy/Reisa Nappe Complexes, e.g. Kirkland *et al.*, 2005; Corfu *et al.*, 2006, 2011).

CONCLUSIONS

This study indicates that the Eidet metasedimentary rocks exposed in the southwestern part of the KNC probably correspond to the Sørøy succession defined farther northeast (e.g. Kirkland *et al.*, 2007b). The combination of structural and microstructural work, phase equilibrium modelling and U–Pb geochronology of several phases demonstrates that the Eidet rocks have experienced at least two high-grade tectonometamorphic events.

(1) A subvertical S1 fabric formed at ~730–775 °C and ~6.3–9.8 kbar, above the wet solidus and overlapping the sillimanite and kyanite stability fields. A U–Pb age of 702 ± 5 Ma from high-U zircon from a leucosome dates partial melting and peak metamorphism. The S1 fabric is therefore pre-Caledonian and the lens-shaped rock body represents a preserved part of the lower crust, which has mostly escaped Caledonian deformational and metamorphic overprint. Monazite grains that grew in this fabric show surprisingly little variation in chemical composition compared to a large spread in (concordant) U–Pb dates from *c.* 800 to 600 Ma. This age spread could either represent protracted growth of monazite during both prograde and retrograde metamorphism, or represent partially reset ages due to diffusion at high temperatures. In both cases, this indicates that elevated temperatures of >600 °C might have lasted for over ~200 Ma from *c.* 800 to 600 Ma.

(2) The S1 fabric is overprinted by a subhorizontal S2 fabric, which formed at ~600–660 °C and ~10–12 kbar where aluminosilicates and monazite were no longer stable for the given bulk rock compositions. The increased amount of white mica in S2 in comparison with S1 suggests that S2 shearing was facilitated by the influx of aqueous fluids. Rutile that originally grew during the S1-forming event lost its Zr signature as well as radiogenic Pb during the S2-forming event and records cooling ages of *c.* 440–420 Ma. Titanite grew at the expense of rutile at slightly lower

temperatures of ~550 °C during later stages of S2 formation and its U–Pb ages of *c*. 440–430 Ma provide a minimum estimate for the age and duration of S2 shearing.

This case study shows the necessity of carefully documenting the link between microstructure, major phase equilibria and mineral composition of geochronometers in order to derive meaningful *P–T–t–d* paths in polymetamorphic crustal sequences. The local preservation of earlier fabrics in lens-shaped rock bodies that escaped re-equilibration during deformation and metamorphism due to fluid deficiency is of great importance for the reconstruction of more complete tectonic histories.

ACKNOWLEDGEMENTS

We thank P. Nasipuri for helpful discussions. Constructive comments by C. Kirkland, an anonymous reviewer and editor D. Robinson improved the manuscript. G. Fjeld is thanked for the help in the TIMS laboratory and S. Simonsen for the help with the LA-ICP-MS analyses at the University of Oslo. SIMS data were collected at the NORDSIM Laboratory, operated under an agreement between the research funding agencies of Denmark, Iceland, Norway and Sweden, the Geological Survey of Finland and the Swedish Museum of Natural History. L. Ilyinsky and K. Lindén assisted with the collection of SIMS data. This is NORDSIM publication #404. P.J. acknowledges the support from the Czech Science Foundation research grant no. 14-25995S, and H.S. support from the University Foundation, Tromsø.

REFERENCES

Bingen, B. & van Breemen, O., 1998. U-Pb monazite ages in amphibolite- to granulite-facies orthogneiss reflect hydrous mineral breakdown reactions: Sveconorwegian Province of SW Norway. *Contributions to Mineralogy and Petrology*, **132,** 336–353.

Cherniak, D.J., 1993. Lead diffusion in titanite and preliminary results on the effects of radiation damage on Pb transport. *Chemical Geology*, **110,** 177–194.

Cherniak, D.J., 2000. Pb diffusion in rutile. *Contributions to Mineralogy and Petrology*, **139,** 198–207.

Cherniak, D.J., 2010. Diffusion in accessory minerals: Zircon, titanite, apatite, monazite and xenotime. In: *Diffusion in Minerals and Melts*. Reviews in Mineralogy and Geochemistry Vol. 72 (eds Zhang, Y. & Cherniak, D.J.), pp. 827–869. Mineralogical Society of America, Chantilly, VA.

Cherniak, D.J., Watson, E.B., Grove, M. & Harrison, T.M., 2004. Pb diffusion in monazite: a combined RBS/SIMS study. *Geochimica et Cosmochimica Acta*, **68,** 829–840.

Cherniak, D.J., Manchester, J. & Watson, E.B., 2007. Zr and Hf diffusion in rutile. *Earth and Planetary Science Letters*, **261,** 267–279.

Coggon, R. & Holland, T.J.B., 2002. Mixing properties of phengitic micas and revised garnet-phengite thermobarometers. *Journal of Metamorphic Geology*, **20,** 683–696.

Connolly, J.A.D., 2005. Computation of phase equilibria by linear programming: a tool for geodynamic modelling and its application to subduction zone decarbonation. *Earth and Planetary Science Letters*, **236,** 524–541.

Copeland, P., Parrish, R.R. & Harrison, T.M., 1988. Identification of inherited radiogenic Pb in monazite and its implications for U-Pb systematics. *Nature*, **333,** 760–763.

Corfu, F., Torsvik, T.H., Andersen, T.B., Ashwal, L.D., Ramsay, D.M. & Roberts, R.J., 2006. Early Silurian mafic-ultramafic and granitic plutonism in contemporaneous flysch, Magerøy, northern Norway: U-Pb ages and regional significance. *Journal of the Geological Society of London*, **163,** 291–301.

Corfu, F., Roberts, R.J., Torsvik, T.H., Ashwal, L.D. & Ramsay, D.M., 2007. Peri-Gondwanan elements in the Caledonian nappes of Finnmark, northern Norway: implications for the paleogeographic framework of the Scandinavian Caledonides. *American Journal of Science*, **307,** 434–458.

Corfu, F., Gerber, M., Andersen, T.B., Torsvik, T.H. & Ashwal, L.D., 2011. Age and significance of Grenvillian and Silurian orogenic events in the Finnmarkian Caledonides, northern Norway. *Canadian Journal of Earth Sciences*, **48,** 419–440.

Daly, J.S., Aitcheson, S.J., Cliff, R.A., Gayer, R.A. & Rice, A.H.N., 1991. Geochronological evidence from discordant plutons from a late Proterozoic orogen in the Caledonides of Finnmark, northern Norway. *Journal of the Geological Society of London*, **148,** 29–40.

Elvevold, S., Reginiussen, H., Krogh, E.J. & Bjørklund, F., 1994. Reworking of deep-seated gabbros and associated contact metamorphosed paragneisses in the south-eastern part of the Seiland Igneous Province, northern Norway. *Journal of Metamorphic Geology*, **12,** 539–556.

Ewing, T.A., Hermann, J. & Rubatto, D., 2013. The robustness of the Zr-in-rutile and Ti-in-zircon thermometers during high-temperature metamorphism (Ivrea-Verbano Zone, northern Italy). *Contributions to Mineralogy and Petrology*, **165,** 757–779.

Ferry, J.M. & Watson, E.B., 2007. New thermodynamic models and revised calibrations for the Ti-in-zircon and Zr-in-rutile thermometers. *Contributions to Mineralogy and Petrology*, **154,** 429–437.

Foster, G. & Parrish, R.R., 2003. Metamorphic monazite and the generation of P–T–t paths. In: *Geochronology: Linking the Isotopic Record with Petrology and Textures* (eds Vance, D., Müller, W. & Villa, I.M.), *Geological Society of London Special Publication*, **220,** 25–47.

Foster, G., Parrish, R.R., Horstwood, M.S.A., Chenery, S., Pyle, J. & Gibson, H.D., 2004. The generation of prograde P–T–t points and paths; a textural, compositional, and chronological study of metamorphic monazite. *Earth and Planetary Science Letters*, **228,** 125–142.

Frost, B.R., Chamberlain, K.R. & Schumacher, J.C., 2000. Sphene (titanite): phase relations and role as a geochronometer. *Chemical Geology*, **172,** 131–148.

Fuhrman, M.L. & Lindsley, H., 1988. Ternary-feldspar modeling and thermometry. *American Mineralogist*, **73,** 201–215.

Gardes, E., Jaoul, O., Montel, J.M., Seydoux-Guillaume, A.M. & Wirth, R., 2006. Pb diffusion in monazite: an experimental study of Pb^{2+} + Th^{4+}-> 2 Nd^{3+} interdiffusion. *Geochimica et Cosmochimica Acta*, **70,** 2325–2336.

Gasser, D., Bruand, E., Rubatto, D. & Stüwe, K., 2012. The behavior of monazite from greenschist facies phyllites to anatectic gneisses: an example from the Chugach Metamorphic Complex, southern Alaska. *Lithos*, **134–135,** 108–122.

Gibson, H.D., Carr, S.D., Brown, R.L. & Hamilton, M.A., 2004. Correlation between chemical and age domains in monazite, and metamorphic reactions involving major pelitic phases: an integration of ID-TIMS and SHRIMP geochronology with Y–Th–U X-ray mapping. *Chemical Geology*, **211,** 237–260.

Harlov, D.E., Wirth, R. & Hetherington, C.J., 2011. Fluid-mediated partial alteration in monazite: the role of coupled dissolution-reprecipitation in element redistribution and mass

transfer. *Contributions to Mineralogy and Petrology*, **162,** 329–348.
Hayden, L.A., Watson, E.B. & Wark, D.A., 2008. A thermobarometer for sphene (titanite). *Contributions to Mineralogy and Petrology*, **155,** 529–540.
Holland, T.J.B. & Powell, R., 1998. An internally consistent thermodynamic data set for phases of petrological interest. *Journal of Metamorphic Geology*, **16,** 309–343.
Holland, T.J.B. & Powell, R., 2001. Calculation of phase relations involving haplogranitic melts using and internally consistent thermodynamic dataset. *Journal of Petrology*, **42,** 673–683.
Janots, E., Brunet, F., Goffé, B., Poinssot, C., Burchard, M. & Cemic, L., 2007. Thermochemistry of monazite-(La) and dissakite-(La): implications for monazite and allanite stability in metapelites. *Contributions to Mineralogy and Petrology*, **154,** 1–14.
Janots, E., Engi, M., Berger, A., Allaz, J., Schwarz, J.O. & Spandler, C., 2008. Prograde metamorphic sequence of REE minerals in pelitic rocks of the Central Alps: implications for allanite–monazite–xenotime phase relations from 250 to 610°C. *Journal of Metamorphic Geology*, **26,** 509–526.
Jeřábek, P., Janák, M., Faryad, S.W., Finger, F. & Konečný, P., 2008. Polymetamorphic evolution of pelitic schists and evidence for Permian low-pressure metamorphism in the Vepor Unit, West Carpathians. *Journal of Metamorphic Geology*, **26,** 465–485.
Jiao, S., Guo, J., Mao, Q. & Zhao, R., 2011. Application of Zr-in-rutile thermometry: a case study from ultrahigh-temperature granulites of the Khondalite belt, North China Craton. *Contributions to Mineralogy and Petrology*, **162,** 379–393.
Kirkland, C.L., Daly, J.S. & Whitehouse, M.J., 2005. Early Silurian magmatism and the Scandian evolution of the Kalak Nappe Complex, Finnmark, Arctic Norway. *Journal of the Geological Society of London*, **162,** 985–1003.
Kirkland, C.L., Daly, J.S. & Whitehouse, M.J., 2006a. Granitic magmatism of Grenvillian and late Neoproterozoic age in Finnmark, Arctic Norway – constraining pre-Scandian deformation in the Kalak Nappe Complex. *Precambrian Research*, **145,** 24–52.
Kirkland, C.L., Daly, J.S., Eide, E.A. & Whitehouse, M.J., 2006b. The structure and timing of lateral escape during the Scandian Orogeny: a combined strain and geochronological investigation in Finnmark, Arctic Norwegian Caledonides. *Tectonophysics*, **425,** 159–189.
Kirkland, C.L., Daly, J.S., Eide, E.A. & Whitehouse, M.J., 2007a. Tectonic evolution of the arctic Norwegian Caledonides from a texturally- and structurally-constrained multi-isotopic (Ar-Ar, Rb-Sr, Sm-Nd, U-Pb) study. *American Journal of Science*, **307,** 459–526.
Kirkland, C.L., Daly, J.S. & Whitehouse, M.J., 2007b. Provenance and terrane evolution of the Kalak Nappe Complex, Norwegian Caledonides: implications for Neoproterozoic Paleogeography and Tectonics. *The Journal of Geology*, **115,** 21–41.
Kirkland, C.L., Daly, J.S., Chew, D.M. & Page, L.M., 2008a. The Finnmarkian Orogeny revisited: an isotopic investigation in eastern Finnmark, Arctic Norway. *Tectonophysics*, **460,** 158–177.
Kirkland, C.L., Daly, J.S. & Whitehouse, M.J., 2008b. Basement-cover relationships of the Kalak Nappe Complex, Arctic Norwegian Caledonides and constraints on Neoproterozoic terrane assembly in the North Atlantic region. *Precambrian Research*, **160,** 245–276.
Kirkland, C.L., Whitehouse, M.J. & Slagstad, T., 2009. Fluid-assisted zircon and monazite growth within a shear zone: a case study from Finnmark, Arctic Norway. *Contributions to Mineralogy and Petrology*, **158,** 637–657.
Kohn, M.J. & Corrie, S.L., 2011. Preserved Zr-temperatures and U-Pb ages in high-grade metamorphic titanite: evidence for a static hot channel in the Himalayan orogen. *Earth and Planetary Science Letters*, **311,** 136–143.
Kohn, M., Wieland, M.S., Parkinson, C.D. & Upreti, B.N., 2005. Five generations of monazite in Langtang gneisses: implications for chronology of the Himalayan metamorphic core. *Journal of Metamorphic Geology*, **23,** 399–406.
Kooijman, E., Mezger, K. & Berndt, J., 2010. Constraints on the U-Pb systematics of metamorphic rutile from in situ LA-ICP-MS analysis. *Earth and Planetary Science Letters*, **293,** 321–330.
Kooijman, E., Smit, M.A., Mezger, K. & Berndt, J., 2012. Trace element systematic in granulite facies rutile: implications for Zr geothermometry and provenance studies. *Journal of Metamorphic Geology*, **30,** 397–412.
Kretz, R., 1983. Symbols of rock-forming minerals. *American Mineralogist*, **68,** 277–279.
Kylander-Clark, A.R.C., Hacker, B.R. & Mattinson, J.M., 2008. Slow exhumation of UHP terranes: titanite and rutile ages of the Western Gneiss Region, Norway. *Earth and Planetary Science Letters*, **272,** 531–540.
Li, Q., Li, S., Zheng, Y.F., Li, H., Massonne, H.J. & Wang, Q., 2003. A high precision U-Pb age of metamorphic rutile in coesite-bearing eclogite from the Dabie Mountains in central China: a new constraint on the cooling history. *Chemical Geology*, **200,** 255–265.
Li, Q., Lin, W., Su, W. *et al*., 2011. SIMS U-Pb rutile age of low-temperature eclogites from southwestern Chinese Tianshan, NW China. *Lithos*, **122,** 76–86.
Lucassen, F., Dulski, P., Abart, R., Franz, G., Rhede, D. & Romer, R.L., 2010. Redistribution of HFSE elements during rutile replacement by titanite. *Contributions to Mineralogy and Petrology*, **160,** 279–295.
Luvizotto, G.L. & Zack, T., 2009. Nb and Zr behaviour in rutile during high-grade metamorphism and retrogression: an example from the Ivrea-Verbano Zone. *Chemical Geology*, **261,** 303–317.
Menegon, L., Nasipuri, P., Stünitz, H., Behrens, H. & Ravna, E., 2011. Dry and strong quartz during deformation of the lower crust in the presence of melt. *Journal of Geophysical Research*, **116,** B10410. doi:10.1029/2011JB008371.
Meyer, M., John, T., Brandt, S. & Klemd, R., 2011. Trace element composition of rutile and the application of Zr-in-rutile thermometry to UHT metamorphism (Epupa Complex, NW Namibia). *Lithos*, **126,** 388–401.
Mezger, K., Hanson, G.N. & Bohlen, S.R., 1989. High-precision U-Pb ages of metamorphic rutile: application to the cooling history of high-grade terranes. *Earth and Planetary Science Letters*, **96,** 106–118.
Mezger, K., Rawnsley, C.M., Bohlen, S.R. & Hanson, G.N., 1991. U-Pb garnet, sphene, monazite, and rutile ages: implications for the duration of high-grade metamorphism and cooling histories, Adironack Mts, New York. *The Journal of Geology*, **99,** 415–428.
Müller, W., 2003. Strengthening the link between geochronology, textures and petrology. *Earth and Planetary Science Letters*, **206,** 237–251.
Parrish, R.R., 1990. U-Pb dating of monazite and its application to geological problems. *Canadian Journal of Earth Sciences*, **27,** 1431–1450.
Paulsson, O. & Andreasson, P.G., 2002. Attempted break-up of Rodinia at 850 Ma: geochronological evidence from the Seve-Kalak Superterrane, Scandinavian Caledonides. *Journal of the Geological Society of London*, **159,** 751–761.
Pyle, J.M. & Spear, F.S., 2003. Four generations of accessory-phase growth in low pressure migmatites from SW New Hampshire. *American Mineralogist*, **88,** 338–351.
Pyle, J.M., Spear, F.S., Rudnick, R.L. & McDonough, W.F., 2001. Monazite-xenotime-garnet equilibrium in metapelites and a new monazite-garnet thermometer. *Journal of Petrology*, **42,** 2083–2107.
Ramsay, D.M., Sturt, B.A., Zwann, K.B. & Roberts, D., 1985. Caledonides of northern Norway. In: *The Caledo-*

nide Orogen – Scandinavia and Related Areas (eds Gee, D.G. & Sturt, B.A.), pp. 163–184. John Wiley & Sons Ltd, Chichester.
Rice, A.H.N. & Frank, W., 2003. The early Caledonian (Finnmarkian) event reassessed in Finnmark: $^{40}Ar/^{39}Ar$ cleavage age data from NW Varangerhalvøya, N. Norway. *Tectonophysics*, **374,** 219–236.
Roberts, D., 2003. The Late Riphean Porsangerhalvøyan tectonometamorphic event in the North Norwegian Caledonides: a comment on nomenclature. *Norwegian Journal of Geology*, **83,** 275–277.
Roberts, R.J., 2007. *The Seiland Igneous Province, Northern Norway: Age, Provenance and Tectonic Significance*. PhD thesis, University of Witwatersrand, 223 pp.
Roberts, D. & Siedlecka, A., 2002. Timanian orogenic deformation along the northeastern margin of Baltica, Northwest Russia and Northeast Norway, and Avalonian-Cadomian connections. *Tectonophysics*, **352,** 169–184.
Roberts, R.J., Corfu, F., Torsvik, T.H., Ashwal, L.D. & Ramsay, D.M., 2006. Short-lived mafic magmatism at 560-570 Ma in the northern Norwegian Caledonides: U-Pb zircon ages from the Seiland Igneous Province. *Geological Magazine*, **143,** 887–903.
Roberts, R.J., Corfu, F., Torsvik, T.H., Hetherington, C.J. & Ashwal, L.D., 2010. Age of alkaline rocks in the Seiland Igneous Province, Northern Norway. *Journal of the Geological Society of London*, **167,** 71–81.
Rubatto, D., 2002. Zircon trace element geochemistry: partitioning with garnet and the link between U-Pb ages and metamorphism. *Chemical Geology*, **184,** 123–138.
Rubatto, D., Williams, I.S. & Buick, I.S., 2001. Zircon and monazite response to prograde metamorphism in the Reynolds Range, central Australia. *Contributions to Mineralogy and Petrology*, **140,** 458–468.
Rubatto, D., Hermann, J. & Buick, I.S., 2006. Temperature and bulk composition control on the growth of monazite and zircon during low-pressure anatexis (Mount Stafford, Central Australia). *Journal of Petrology*, **47,** 1973–1996.
Schuster, R. & Stüwe, K., 2008. Permian metamorphic event in the Alps. *Geology*, **36,** 603–606.
Seydoux-Guillaume, A.M., Paquette, J.L., Wiedenbeck, M., Montel, J.M. & Heinrich, W., 2002. Experimental resetting of the U-Th-Pb systems in monazite. *Chemical Geology*, **191,** 165–181.
Siedlecka, A., Roberts, D., Nystuen, J.P. & Olovyanishnikov, V.G., 2004. Northeastern and northwestern margins of Baltica in Neoproterozoic time: evidence from the Timanian and Caledonian orogens. In: *The Neoproterozoic Timanide Orogen of Eastern Baltica* (eds Gee, D.G. & Pease, V.), *Geological Society of London Memoirs*, **30,** 169–190.
Slagstad, T., Melezhik, V.A., Kirkland, C.L. *et al*., 2006. Carbonate isotope chemostratigraphy suggests revisions to the geological history of the West Finnmark Caledonides, northern Norway. *Journal of the Geological Society of London*, **163,** 277–289.
Slàma, J., Kosler, J. & Pedersen, R.B., 2007. Behaviour of zircon in high-grade metamorphic rocks: evidence from Hf isotopes, trace elements and textural studies. *Contributions to Mineralogy and Petrology*, **154,** 335–356.
Smith, H.A. & Barreiro, B., 1990. Monazite U–Pb dating of staurolite-grade metamorphism in pelitic schists. *Contributions to Mineralogy and Petrology*, **105,** 602–615.
Smith, H.A. & Giletti, B.J., 1997. Lead diffusion in monazite. *Geochimica et Cosmochimica Acta*, **61,** 1047–1055.
Spear, F.S., 2010. Monazite–allanite phase relations in metapelites. *Chemical Geology*, **279,** 55–62.
Sturt, B.A., Pringle, I.R. & Ramsay, D.M., 1978. The Finnmarkian phase of the Caledonian Orogeny. *Journal of the Geological Society of London*, **135,** 597–610.
Sundvoll, B. & Roberts, D., 2003. A likely Ordovician age for the regional, penetrative cleavage in the Gaissa Nappe Complex, northern Norway. *Norges Geologiske Undersøkelse Bulletin*, **441,** 51–59.
Suzuki, K., Adachi, M. & Kajizuka, I., 1994. Electron microprobe observations of Pb diffusion in metamorphosed detrital monazites. *Earth and Planetary Science Letters*, **128,** 391–405.
Tajčmanová, L., Connolly, J.A.D. & Cesare, B., 2009. A thermodynamic model for titanium and ferric iron solution in biotite. *Journal of Metamorphic Geology*, **27,** 153–165.
Teufel, S. & Heinrich, W., 1997. Partial resetting of the U-Pb isotope system in monazite through hydrothermal experiments: an SEM and U–Pb isotope study. *Chemical Geology*, **137,** 273–281.
Tomkins, H.S., Powell, R. & Ellis, D.J., 2007. The pressure dependence of the zirconium-in-rutile thermometer. *Journal of Metamorphic Geology*, **25,** 703–713.
Vry, J.K. & Baker, J.A., 2006. LA-MC-ICPMS Pb-Pb dating of rutile from slowly cooled granulites: confirmation of the high closure temperature for Pb diffusion in rutile. *Geochimica et Cosmochimica Acta*, **70,** 1807–1820.
Warren, C.J., Grujic, D., Cottle, J.M. & Rogers, N.W., 2012. Constraining cooling histories: rutile and titanite chronology and diffusion modeling in NW Bhutan. *Journal of Metamorphic Geology*, **30,** 113–130.
Watson, E.B. & Harrison, T.M., 2005. Zircon thermometer reveals minimum melting conditions on earliest Earth. *Science*, **308,** 841–844.
Watson, E.B., Wark, D.A. & Thomas, J.B., 2006. Crystallization thermometers for zircon and rutile. *Contributions to Mineralogy and Petrology*, **151,** 413–433.
Williams, M.L., Jercinovic, M.J. & Hetherington, J., 2007. Microprobe monazite geochronology: understanding geologic processes by integrating composition and chronology. *Annual Reviews in Earth and Planetary Sciences*, **35,** 137–175.
Williams, M.L., Jercinovic, M.J., Harlov, D.E., Budzyn, B. & Hetherington, C.J., 2011. Resetting monazite ages during fluid-related alteration. *Chemical Geology*, **283,** 218–225.
Wing, B.A., Ferry, J.M. & Harrison, T.M., 2003. Prograde destruction and formation of monazite and allanite during contact and regional metamorphism of pelites: petrology and geochronology. *Contributions to Mineralogy and Petrology*, **145,** 28–250.
Zack, T., Moraes, R. & Kronz, A., 2004. Temperature dependence of Zr in rutile: empirical calibration of a rutile thermometer. *Contributions to Mineralogy and Petrology*, **148,** 471–488.
Zhu, X.K. & O'Nions, R.K., 1999. Zonation of monazite in metamorphic rocks and its implications for high temperature thermochronology: a case study from the Lewisian terrain. *Earth and Planetary Science Letters*, **171,** 209–220.
Zwaan, K.B., 1988. Nordreisa. Bedrock geology map 1:250 000. Geological Survey of Norway.

SUPPORTING INFORMATION

Additional Supporting Information may be found in the online version of this article at the publisher's web site:

Appendix S1. Analytical methods.

Table S1. Representative garnet compositions.

Table S2. Representative muscovite, biotite and plagioclase compositions.

Table S3. Trace element composition of rutile derived by EMPA and Zr-in-rutile thermometry.

Table S4. U–Pb LA-ICP-MS results for sample Sk3a (detrital zircon).

Table S5. SIMS U–Th–Pb zircon data for leucosome sample Sk3c.

Table S6. Representative monazite EMP analyses.

Table S7. SIMS U–Th–Pb monazite data for leucosome sample Sk3c and melanosome sample Sk3d.

Table S8. U–Pb TIMS data, rutile and titanite.

Received 17 October 2014; revision accepted 24 March 2015.

Supplementary information for:

PAPER I

Behaviour of geochronometers and timing of metamorphic reactions during deformation at lower crustal conditions: Phase equilibrium modelling and U-Pb dating of zircon, monazite, rutile and titanite from the Kalak Nappe Complex, northern Norway

Gasser, D.[1], Jeřábek, P.[2], Faber, C.[3], Stünitz, H.[3], Menegon, L.[4], Corfu, F.[5], Erambert, M.[5], Whitehouse, M.J.[6]

Table S1: Representative garnet compositions.

Table S2: Representative muscovite, biotite and plagioclase compositions.

Table S3: Trace element composition of rutile derived EMPA and Zr-in-rutile thermometry.

Table S4: U-Pb LA-ICP-MS results for sample Sk3a (detrital zircon).

Table S5: SIMS U-Th-Pb zircon data for leucosome sample Sk3c.

Table S6: Representative monazite EMP analyses.

Table S7: SIMS U-Th-Pb monazite data for leucosome sample Sk3c and melanosome sample Sk3d.

SUPPORTING INFORMATION FOR:

Behaviour of geochronometers and timing of metamorphic reactions during deformation at lower crustal conditions: Phase equilibrium modelling and U-Pb dating of zircon, monazite, rutile and titanite from the Kalak Nappe Complex, northern Norway

Gasser, D.[1], Jeřábek, P.[2], Faber, C.[3], Stünitz, H.[3], Menegon, L.[4], Corfu, F.[5], Erambert, M.[5], Whitehouse, M.J.[6]

[1]Geological Survey of Norway, Leiv Eirikssons vei 39, 7491 Trondheim, Norway (deta.gasser@ngu.no)

[2]Institute of Petrology and Structural Geology, Charles University, 128 43 Praha 2, Czech Republic

[3]Department of Geology, University of Tromsø, Dramsveien 201, 9037 Tromsø, Norway

[4]School of Geography, Earth and Environmental Sciences, Plymouth University, Fitzroy, Drake Circus, Plymouth, Devon, PL4 8AA, United Kingdom

[5]Department of Geosciences, University of Oslo, Postbox 1047, Blindern, 0316 Oslo, Norway

[6]Department of Geosciences, Swedish Museum of Natural History, Box 50007, SE-104 05Stockholm, Sweden

APPENDIX S1 - ANALYTICAL METHODS

The bulk rock chemical composition of the investigated samples was determined by standard x-ray fluorescence (XRF) analysis, using a Bruker S8 Tiger XRF, of fused glass beads with 1:8 dilution of the rock powder with Li-tetraborate.

Polished thin sections were investigated by light microscopy. All microprobe analyses were carried out in WDS mode using the CAMECA SX100 electron microprobe (EMP) at the Department of Geosciences, University of Oslo, Norway, and all matrix corrections were done according to the PAP procedure (Pouchou & Pichoir, 1984), implemented in the CAMECA software. Garnet, biotite and white mica were analyzed for major element chemistry using an accelerating voltage of 15 kV, a beam current of 15 nA, a focussed beam and a counting time on peak of 10 s (and 5 s on each of the background positions). Na and K were analysed first. The element maps of garnet were done using the scanning electron microscope TESCAN Vega with energy-dispersive spectrometer X-MAX 50 (Oxford Instruments) at the Institute of Petrology and Structural Geology, Charles University in Prague. The analyses were obtained with an accelerating potential of 15 kV and a beam current of 1 nA.

Identification and high-contrast back-scattered electron (BSE) imaging of monazite was done on polished thin sections and mineral mounts with a JEOL scanning electron microscope, working at 15 kV, ~6 nA and 15 mm working distance. Quantitative EMP

analyses of monazite were obtained using an accelerating voltage of 20 kV, a beam current of 20 nA and a beam diameter of 5 to 10 μm. Peak counting times ranged from 20s to 40 s. Calibration standards and x-ray lines used were wollastonite (Si Kα, Ca Kα), synthetic REE orthophosphates from Jarosewich & Boatner (1991) for Y, REE and P (P Kα, La Lα, Ce Lα, Pr Lβ, Nd Lβ, Gd Lβ), Sm-Y-Tb oxide (Sm Lβ), Si-Al-Ca glasses with 15 wt% Th (Th Mα) and 15 wt % U (U Mβ). Pb was not analysed. All analyses were performed in differential mode (e.g. pulse height analysis) to remove possible interferences of multiple-order x-ray lines.

EMP trace element analyses (Ti, Zr, Si, Fe, Nb, Cr) of rutile were obtained on polished thin sections. The analytical conditions were accelerating voltage 20 kV, beam current 100 nA, and counting time of 120s on peak for all elements (and 60s on each of the two background positions). As for monazite, all elements (except Si for rutile) were performed in differential mode. Background positions were selected on detailed WDS scans around the x-ray lines of interest. The following X-ray line/ spectrometer crystal/ calibration standard were used: Fe Kα / LIF / metal Fe, Zr Lα / LTAP / Monastery Mine zircon, Nb Lα / LPET / metal Nb, Cr Kα / LLIF / synthetic Cr2O3, Si Kα / TAP / wollastonite.

For geochronology, zircon, monazite, titanite and rutile were separated from the samples using standard crushing and mineral separation techniques, followed by hand-picking of the grains under a binocular microscope. Magnetic separation was not used for the detrital zircon sample in order to avoid bias in the zircon selection. Zircon and monazite grains selected for LA-ICP-MS and ion probe analysis were mounted in epoxy, polished to expose the core of the grains, and imaged by CL with a JEOL scanning electron microscope.

U-Pb LA-ICP-MS analyses on detrital zircon were performed using a Nu Plasma HR multicollector ICP-MS system and a New Wave/Merchantek LUV-213 laser microprobe, using a standardization method described by Rosa *et al.* (2009). Masses 204, 206, 207 and 238 were measured simultaneously and ^{235}U was calculated from ^{238}U using a natural $^{238}U/^{235}U$=137.88. Mass number 204 was used as a monitor for ^{204}Pb. The reference zircons GJ-01 (609±1 Ma; Belusova *et al.*, 2006), 91500 (1065±1 Ma, Wiedenbeck *et al.*, 1995) and the in-house standard A382 (1876±5 Ma) were used. No common Pb correction was applied (Table S4). Data reduction was performed using an interactive, in-house Microsoft Excel 2003 spreadsheet program written by T. Andersen and age calculation was done using Isoplot/Ex 4.1 (Ludwig, pers. Comm.). For age probability plots, $^{207}Pb/^{206}Pb$ ages are used and for statistical analysis, a Kolmogorov–Smirnov (K–S) statistical test was applied using the Excel macro developed by the Arizona LaserChron Center.

Secondary ion mass spectrometer (SIMS) U-Th-Pb analyses of zircon and monazite were carried out using a large geometry CAMECA IMS1280 instrument (Nordsim facility). Basic instrument set-up broadly follows that described by Whitehouse & Kamber (2005) and references therein. An O_2^- primary beam with 23 kV incident energy (-13kV primary, +10 kV secondary) was used to sputter both minerals, with the primary beam operated in aperture illumination (Köhler) mode yielding a ~15-20 μm spot which was presputtered using a 25 μm raster for 90 s to remove gold and minimise surface contamination. For zircon, centring of the secondary ion beam in the 4000 μm field aperture (FA), mass calibration optimisation, and optimisation of the secondary beam energy distribution in the 45eV energy window were performed automatically for each run using the $^{90}Zr_2{}^{16}O+$ species at nominal mass 196. Mass calibration of all peaks in the mono-collection sequence was performed at the start of each analytical session; while within run mass calibration optimisation scanned only $^{90}Zr_2{}^{16}O$ + to adjust the mass calibration slope to account for small drift. A mass resolution (M/ΔM) of ~5400 was used to ensure adequate separation of Pb isotope peaks from nearby $HfSi^+$ species. Ion signals were detected using the axial ion-counting electron multiplier. All analyses were run in fully automated chain sequences. Zircon data reduction assumes a power law

relationship between Pb^+/U^+ and UO_2^+/U^+ ratios with an empirically derived slope in order to calculate actual Pb/U ratios based on those in the 91500 reference zircon. The U concentration and Th/U ratio are also referenced to the Geostandards 91500 zircon, which has a $^{207}Pb/^{206}Pb$ age of 1065 Ma (Wiedenbeck *et al.*, 1995).

Monazite U-Th-Pb analyses by SIMS used the same instrument and similar operating parameters with regard to primary beam and mass resolution to those used for zircon, broadly following the protocols described in Kirkland *et al.* (2009). The principal difference is that the monazite analyses employed both a smaller entrance slit (30 µm instead of 75 µm) to limit the secondary beam intensity, as well as a smaller energy slit (30 eV instead of 45 eV) together with a -30 eV energy offset (applied via sample high voltage) on all the Pb, ThO_x and UO_x (where x = 0, 1 or 2) peaks of interest in order to minimise matrix differences in potentially chemically diverse monazite, and eliminate a small $ThNdO_2^{2+}$ interference on ^{204}Pb identified in earlier monazite studies (e.g. Kirkland *et al.*, 2009). Secondary beam centring and optimisation steps were performed as for zircon, but using the $CePO_2^+$ matrix peak at nominal mass 203. U-Pb ratios were calibrated against a 425 Ma reference monazite from a metapelite of the Wilmington Complex, Delaware (sample 44069, Aleinikoff *et al*., 2006), using a simple one-dimensional calibration approach, i.e. $(Pb/U)_{true} = k.(Pb/UO2)_{meas}$ where k is an empirical derived constant from the measurement of these ratios in the reference monazite (e.g. Fletcher *et al.,* 2010).

For both zircon and monazite, common Pb corrections were made only when ^{204}Pb counts statistically exceed average background and assume a $^{207}Pb/^{206}Pb$ ratio of 0.83 (equivalent to present day Stacey & Kramers (1975) model terrestrial Pb). Age interpretations use the routines of Isoplot/Ex (Ludwig, 2001). Decay constants follow the recommendations of Steiger & Jäger (1977).

For U-Pb TIMS analyses of titanite and rutile, minerals were washed in dilute HNO_3, ionized water and acetone using an ultrasonic bath in order to remove any contamination. Each sample was weighed on a microbalance and spiked with a mixed ^{202}Pb - ^{205}Pb - ^{235}U tracer. The samples were then dissolved in HF and a drop of HNO_3 in teflon bombs in an oven at ~ 195 °C (rutile) and savillex vials on a hot-plate (titanite) for five days. The solutions were chemically separated using micro-columns and anion-exchange resin in order to remove cations that may inhibit ionization (Krogh, 1973). The U-Pb-solutions were dried down and loaded on degassed single Re filaments with silica gel and measured on a Finnigan MAT 262 mass spectrometer. Details on the measuring process are given in Appendix A of Augland *et al.* (2010). The analytical errors and corrections were incorporated and propagated using an in-house program (ROMAGE 6.3). Since titanite and rutile contain more common Pb than zircon and monazite, the common Pb for titanite and rutile was corrected using the lead composition of co-existing plagioclase (Table S8).

For all age interpretations, the routines of ISOPLOT 4.1 were used (Ludwig, 2001; Ludwig, personal communication). Decay constants follow the recommendations of Steiger & Jäger (1977).

REFERENCES

Aleinikoff, J.N., Schenck, W.S., Plank, M.O., Srogi, L., Fanning, C.M., Kamo, S.L. & Bosbyshell, H., 2006. Deciphering igneous and metamorphic events in high-grade rocks of the Wilmington Complex, Delaware: Morphology, cathodoluminescence and backscattered electron zoning, and SHRIMP U-Pb geochronology of zircon and monazite. *Geological Society of America Bulletin*, **118**, 39-64

Augland, L.E., Andresen, A. & Corfu, F., 2010. Age, structural setting, and exhumation of the Liverpool Land eclogite terrane, East Greenland Caledonides. *Lithosphere,* **2**, 267-286.

Belousova, E. A., Griffin, W.L. & O'Reilly, S.Y., 2006. Zircon crystal morphology, trace element signatures and Hf isotope composition as a tool for petrogenetic modeling: examples from Eastern Australian granitoids. *Journal of Petrology*, **47**, 329–353

Fletcher, I.R., McNaughton, N.J., Davis, W.J. & Rasmussen, B., 2010. Matrix effects and calibration limitations in ion probe U-Pb and Th-Pb dating of monazite. *Chemical Geology*, **270**, 31-44.

Jarosewich, E. & Boatner, L.A., 1991. Rare-earth element reference samples for electron microprobe analysis. *Geostandards Newsletter*, **15**, 397-399.

Kirkland, C.L., Whitehouse, M.J. & Slagstad, T., 2009. Fluid-assisted zircon and monazite growth within a shear zone: a case study from Finnmark, Arctic Norway. *Contributions to Mineralogy and Petrology*, **158**, 637-657.

Krogh, T.E., 1973. A low-contamination method for hydrothermal decomposition of zircon and extraction of U and Pb for isotopic age determination. *Geochimica et Cosmochimica Acta*, **37**, 485–494.

Ludwig, K.R., 2001, Isoplot/Ex, rev. 2.49. A Geochronological Toolkit for Microsoft Excel: Berkeley Geochronology Center, Special Publication No. 1a.

Pouchou, J. & Pichoir, F., 1984. A new model for quantitative X-ray microanalysis; Part 1. Application to the analysis of homogenous samples. *Recherche Aerospatiale*, **3**, 13-38.

Rosa, D.R.N., Finch, A.A., Andersen, T. & Inverno, C.M.C., 2009. U–Pb geochronology and Hf isotope ratios of magmatic zircons from the Iberian Pyrite Belt. *Contributions to Mineralogy and Petrology*, **95**, 47–69.

Stacey, J.S. & Kramers, J.D., 1975. Approximation of terrestrial lead isotope evolution by a 2-stage model. *Earth and Planetary Science Letters*, **26**, 207-221.

Steiger, R.H. & Jäger, E., 1977. Subcommission on geochronology: convention of the use of decay constants in geo- and cosmochronology. *Earth and Planetary Science Letters*, **36**, 359-362.

Wiedenbeck, M., Allé, P., Corfu, F., Griffin, W.L., Meier, M., Oberli, F., von Quadt, A., Roddick, J. C. & Spiegel, W., 1995. Three natural zircon standards for U-Th-Pb, Lu-Hf, trace element and REE analysis. *Geostandards Newsletter*, **19**, 1- 23.

Whitehouse, M.J. & Kamber, B., 2005. Assigning dates to thin gneissic veins in high-grade metamorphic terranes: a cautionary tale from Akilia, southwest Greenland. *Journal of Petrology*, **46**, 291-318.

Table S1. Representative garnet compositions

Mineral	Grt																							
Fabric	S1												S2											
Sample	S18a						S18f						S18b						S18d					
	Core	Rim	Core	Rim	Core	Rim	Core	Rim	Core	Rim	Core	Rim	Core	Rim	Core	Rim	Core	Rim	Core	Rim	Core	Rim	Core	Rim
Wt%																								
SiO_2	37.14	37.19	37.47	37.40	37.65	37.79	37.19	37.46	37.57	37.79	37.44	36.86	36.95	37.36	36.81	37.56	37.29	37.30	36.91	37.63	37.28	38.09	37.64	37.89
TiO_2	0.01	0.02	0.00	0.01	0.01	-0.19	0.03	-0.01	0.02	0.02	0.01	0.01	0.00	0.01	0.03	0.01	0.03	0.00	0.00	0.03	0.04	0.00	0.00	0.01
Al_2O_3	21.09	21.32	21.21	21.42	21.34	21.41	21.27	21.12	21.17	21.22	21.10	21.27	21.08	21.14	21.12	21.24	21.29	21.38	20.74	20.85	20.91	21.51	21.09	20.98
Fe_2O_3	0.05	0.00	1.00	0.62	0.00	0.03	0.00	0.01	0.00	0.00	0.23	1.69	1.33	1.26	1.05	0.37	0.84	0.32	1.32	0.55	0.11	0.00	0.00	0.11
FeO	34.40	34.17	33.46	33.34	33.86	33.42	34.18	34.51	34.20	33.81	34.23	32.89	33.37	29.07	33.38	29.66	32.80	29.75	27.46	28.72	27.27	30.11	27.59	29.30
MnO	1.31	1.36	1.62	1.54	1.47	1.01	2.02	1.74	1.43	1.03	1.42	1.33	1.50	0.69	2.17	0.75	1.49	0.86	8.34	4.53	8.34	2.42	8.45	2.74
MgO	3.93	3.98	4.35	4.25	4.03	3.93	3.78	3.91	4.02	3.88	3.88	4.03	3.58	2.47	3.94	2.61	3.49	2.42	3.36	3.39	3.63	3.33	3.53	3.16
CaO	1.30	1.21	1.37	1.72	1.81	2.67	1.12	1.14	1.42	2.49	1.73	2.00	2.12	8.09	1.11	7.57	3.00	7.52	1.66	4.26	1.80	4.91	1.96	5.78
Total	99.22	99.25	100.47	100.29	100.17	100.06	99.60	99.89	99.83	100.24	100.03	100.07	99.93	100.10	99.62	99.77	100.23	99.54	99.79	99.95	99.38	100.37	100.27	99.98
Si	3.00	2.99	2.98	2.98	3.00	3.01	2.99	3.00	3.01	3.01	3.00	2.95	2.97	2.97	2.96	2.99	2.97	2.98	2.98	3.00	3.00	3.02	3.01	3.02
Ti	0.00	0.00	0.00	0.00	0.00	-0.01	0.00	0.00	0.00	0.00	0.00	0.00	0.00	0.00	0.00	0.00	0.00	0.00	0.00	0.00	0.00	0.00	0.00	0.00
Al	2.01	2.02	1.99	2.01	2.00	2.01	2.02	2.00	2.00	1.99	1.99	2.00	1.99	1.98	2.00	2.00	2.00	2.02	1.97	1.96	1.99	2.01	1.99	1.97
Fe^{3+}	0.00	0.00	0.06	0.04	0.00	0.00	0.00	0.00	0.00	0.00	0.01	0.10	0.08	0.08	0.06	0.02	0.05	0.02	0.08	0.03	0.01	0.00	0.00	0.01
Fe^{2+}	2.32	2.30	2.22	2.22	2.26	2.22	2.30	2.31	2.29	2.25	2.29	2.20	2.24	1.93	2.25	1.98	2.19	1.99	1.85	1.92	1.84	2.00	1.84	1.95
Mn	0.09	0.09	0.11	0.10	0.10	0.07	0.14	0.12	0.10	0.07	0.10	0.09	0.10	0.05	0.15	0.05	0.10	0.06	0.57	0.31	0.57	0.16	0.57	0.18
Mg	0.47	0.48	0.52	0.50	0.48	0.47	0.45	0.47	0.48	0.46	0.46	0.48	0.43	0.29	0.47	0.31	0.41	0.29	0.40	0.40	0.44	0.39	0.42	0.37
Ca	0.11	0.10	0.12	0.15	0.15	0.23	0.10	0.10	0.12	0.21	0.15	0.17	0.18	0.69	0.10	0.65	0.26	0.64	0.14	0.36	0.16	0.42	0.17	0.49
X_{alm}	0.78	0.77	0.75	0.75	0.75	0.74	0.77	0.77	0.77	0.75	0.76	0.75	0.76	0.65	0.76	0.66	0.74	0.67	0.62	0.64	0.61	0.67	0.61	0.65
X_{prp}	0.16	0.16	0.17	0.17	0.16	0.16	0.15	0.16	0.16	0.15	0.15	0.16	0.14	0.10	0.16	0.10	0.14	0.10	0.14	0.13	0.15	0.13	0.14	0.12
X_{sps}	0.03	0.03	0.04	0.03	0.03	0.02	0.05	0.04	0.03	0.02	0.03	0.03	0.03	0.02	0.05	0.02	0.03	0.02	0.19	0.10	0.19	0.05	0.19	0.06
X_{grs}	0.04	0.03	0.04	0.05	0.05	0.08	0.03	0.03	0.04	0.07	0.05	0.06	0.06	0.23	0.03	0.22	0.09	0.22	0.05	0.12	0.05	0.14	0.06	0.16
X_{Mg}	0.17	0.17	0.19	0.19	0.17	0.17	0.16	0.17	0.17	0.17	0.17	0.18	0.16	0.13	0.17	0.14	0.16	0.13	0.18	0.17	0.19	0.16	0.19	0.16

Table S2. Representative muscovite, biotite and plagioclase compositions.

Mineral	Muscovite								Biotite										Plagioclase							
Fabric	S1				S2				S1						S2				S1				S2			
Sample	S18a	S18a	S18f	S18f	S18b	S18b	S18d	S18d	S18a	S18a	S18f	S18f	S18f	S18b	S18b	S18b	S18d	S18d	S18a	S18a	S18f	S18f	S18b	S18b	S18d	S18d
													Incl. in grt			Incl. In grt											
Wt%																										
SiO_2	45.84	45.72	46.23	46.10	45.58	46.91	45.81	46.00	36.44	36.14	35.99	36.21	36.43	36.11	36.13	35.92	36.45	36.48	61.27	61.80	61.23	60.21	62.75	62.81	62.52	62.21
TiO_2	1.80	1.89	1.47	1.44	0.60	1.22	0.86	0.91	4.01	4.31	4.33	4.74	5.47	2.70	2.77	4.62	2.17	2.48	0.00	0.00	0.00	0.02	0.01	0.00	0.00	0.00
Cr_2O_3	0.04	0.04	0.02	0.04	0.02	0.03	0.00	0.02	0.03	0.02	0.02	-0.02	0.03	0.03	0.05	0.07	0.02	0.01	0.02	0.00	0.00	0.01	0.00	0.01	0.01	0.00
Al_2O_3	33.89	33.79	34.62	34.66	34.14	32.09	31.73	30.62	17.39	17.46	17.85	17.61	18.04	16.93	17.15	17.36	16.73	16.26	23.86	24.03	24.04	23.68	23.16	23.24	23.43	23.44
Fe_2O_3	0.00	0.00	0.00	0.00	0.00	0.32	2.28	3.40	0.00	0.00	0.00	0.00	0.00	0.00	0.00	0.00	0.00	0.00	0.00	0.09	0.03	0.08	0.02	0.00	0.06	0.04
FeO	1.38	1.07	1.39	1.36	1.89	1.79	1.72	0.76	16.93	16.87	18.62	17.21	16.02	18.63	18.76	16.53	18.64	19.28	0.00	0.00	0.00	0.00	0.00	0.06	0.00	0.00
MnO	0.04	0.00	0.00	0.03	0.00	0.02	0.03	0.01	0.05	0.04	0.09	0.02	0.00	0.04	0.02	0.03	0.04	0.05	0.00	0.02	0.00	0.00	0.02	0.00	0.00	0.00
MgO	1.20	1.12	1.18	1.06	1.23	1.87	1.34	1.51	10.42	10.33	8.67	9.09	9.96	10.07	9.93	10.31	10.94	10.35	0.00	0.01	0.00	0.01	0.01	0.01	0.00	0.00
CaO	0.00	0.00	0.00	0.00	0.00	0.00	0.00	0.00	0.01	0.00	0.00	0.00	0.00	0.00	0.00	0.00	0.00	0.00	5.65	5.70	5.81	5.75	4.68	4.83	5.02	5.26
Na_2O	0.41	0.37	0.37	0.42	0.62	0.58	0.65	0.68	0.11	0.08	0.06	0.07	0.12	0.13	0.15	0.32	0.18	0.18	8.40	8.40	8.33	8.16	8.97	8.89	8.97	8.82
K_2O	10.70	10.79	10.83	10.61	9.86	10.35	10.12	10.40	9.68	9.68	9.80	9.77	9.74	9.32	9.26	9.04	9.54	9.38	0.23	0.25	0.22	0.24	0.17	0.10	0.07	0.11
Total	95.31	94.79	96.11	95.72	93.94	95.17	94.54	94.30	95.07	94.93	95.42	94.71	95.81	93.97	94.22	94.21	94.71	94.49	99.42	100.30	99.67	98.16	99.80	99.95	100.09	99.87
Si	3.07	3.08	3.06	3.07	3.08	3.14	3.11	3.13	2.85	2.83	2.84	2.87	2.84	2.86	2.86	2.84	2.85	2.88	2.74	2.74	2.73	2.73	2.78	2.78	2.77	2.76
Ti	0.09	0.10	0.07	0.07	0.03	0.06	0.04	0.05	0.24	0.25	0.26	0.28	0.32	0.16	0.16	0.27	0.13	0.15	0.00	0.00	0.00	0.00	0.00	0.00	0.00	0.00
Cr	0.00	0.00	0.00	0.00	0.00	0.00	0.00	0.00	0.00	0.00	0.00	0.00	0.00	0.00	0.00	0.00	0.00	0.00	0.00	0.00	0.00	0.00	0.00	0.00	0.00	0.00
Al	2.67	2.68	2.71	2.72	2.72	2.53	2.54	2.46	1.60	1.61	1.66	1.64	1.66	1.58	1.60	1.62	1.54	1.51	1.26	1.25	1.26	1.26	1.21	1.21	1.22	1.23
Fe^{3+}	0.00	0.00	0.00	0.00	0.00	0.02	0.12	0.17	0.00	0.00	0.00	0.00	0.00	0.00	0.00	0.00	0.00	0.00	0.00	0.00	0.00	0.00	0.00	0.00	0.00	0.00
Fe^{2+}	0.08	0.06	0.08	0.08	0.11	0.10	0.10	0.04	1.10	1.11	1.23	1.14	1.04	1.24	1.24	1.09	1.22	1.27	0.00	0.00	0.00	0.00	0.00	0.00	0.00	0.00
Mn	0.00	0.00	0.00	0.00	0.00	0.00	0.00	0.00	0.00	0.00	0.01	0.00	0.00	0.00	0.00	0.00	0.00	0.00	0.00	0.00	0.00	0.00	0.00	0.00	0.00	0.00
Mg	0.12	0.11	0.12	0.10	0.12	0.19	0.14	0.15	1.21	1.21	1.02	1.07	1.16	1.19	1.17	1.21	1.28	1.22	0.00	0.00	0.00	0.00	0.00	0.00	0.00	0.00
Ca	0.00	0.00	0.00	0.00	0.00	0.00	0.00	0.00	0.00	0.00	0.00	0.00	0.00	0.00	0.00	0.00	0.00	0.00	0.27	0.27	0.28	0.28	0.22	0.23	0.24	0.25
Na	0.05	0.05	0.05	0.05	0.08	0.08	0.09	0.09	0.02	0.01	0.01	0.01	0.02	0.02	0.02	0.05	0.03	0.03	0.73	0.72	0.72	0.72	0.77	0.76	0.77	0.76
K	0.91	0.93	0.92	0.90	0.85	0.88	0.88	0.90	0.97	0.97	0.99	0.99	0.97	0.94	0.94	0.91	0.95	0.94	0.01	0.01	0.01	0.01	0.01	0.01	0.00	0.01
X_{Mg}									0.53	0.52	0.45	0.48	0.53	# 0.49	0.49	0.53	0.51	0.49								
An %																			27	27	27	28	22	23	23	25

Table S3. Trace element composition of rutile derived by EMPA and Zr-in-rutile thermometry

Point#	Grain-Nr	Zr(ppm)	±2σ (ppm)	Cr	Nb	Si	Fe	Zr-in-rutile termometry (°C) Tomkins et al. 2007 β-quartz field	±2σ (°C) only analytical
Sample Sk3d (subvertical fabric)									
~~7~~	4	~~86~~	~~30~~	~~271~~	~~1756~~	~~40769~~	~~82236~~	~~554~~	~~19/26~~
29	17	92	31	351	3373	473	2683	558	19/26
11	7	100	31	330	3579	861	5002	563	18/23
25	16	101	31	396	5506	369	4288	564	18/23
26	16	108	31	412	6294	338	5438	568	17/22
12	8	113	31	352	4014	290	3030	571	16/21
45	25	125	31	348	1809	237	2551	578	15/19
35	19	128	32	291	4157	274	4228	580	15/19
~~51~~	~~28~~	~~130~~	~~31~~	~~316~~	~~3288~~	~~1734~~	~~4382~~	~~581~~	~~15/18~~
48	27	131	31	332	1568	269	4674	581	15/18
32	17	133	31	298	2057	485	2781	582	14/18
23	15	137	31	323	1822	608	3651	584	14/17
31	17	140	31	335	2137	406	2394	586	14/17
49	27	140	31	341	2803	236	5520	586	14/17
34	18	142	31	218	1908	434	2399	587	14/17
37	20	146	32	332	3843	418	3987	589	14/17
50	28	146	31	331	3086	259	3682	589	13/16
36	19	147	32	281	3549	365	3705	589	14/17
46	26	150	31	338	2999	480	2673	590	13/16
47	26	150	31	371	2636	330	3197	590	13/16
15	10	155	31	312	2628	466	2902	593	13/15
43	23	157	31	344	3206	471	2419	594	13/15
~~2~~	~~1~~	~~159~~	~~31~~	~~459~~	~~6809~~	~~10196~~	~~4045~~	~~594~~	~~13/15~~
24	15	159	31	320	1708	717	2623	594	13/15
27	16	159	31	400	5269	483	3588	594	13/15
28	16	159	31	381	5455	538	3576	594	13/15
16	11	160	31	338	1716	201	1653	595	13/15
38	20	161	31	321	3308	442	2944	595	13/15
33	18	166	31	226	1803	364	2355	597	12/14
40	21	166	31	319	4055	297	2618	597	12/14
21	14	170	31	383	2856	371	3371	599	12/14
22	14	171	31	363	2887	493	3611	600	12/14
20	13	172	31	296	2326	862	3313	600	12/14
30	17	173	31	366	2497	337	2371	600	12/14
39	20	177	31	327	3188	462	2725	602	12/13
8	5	178	32	358	2870	191	3235	602	12/14
13	9	178	31	365	7273	240	4000	602	12/13
1	1	185	31	462	7218	600	3760	605	11/13
14	10	187	31	356	3156	310	2664	606	11/13
44	24	187	31	363	3356	192	2392	606	11/13
41	22	196	31	321	2041	431	2403	609	11/12
6	4	198	32	387	3641	551	7898	610	11/13
3	2	199	31	349	3425	95	2730	610	11/12
5	3	200	31	383	4176	311	3689	611	11/12
10	6	202	31	289	4525	203	3714	612	11/12

42	23	202	32	400	5104	417	2927	612	11/12
4	3	206	31	389	4030	226	3213	613	10/12
9	5	208	32	351	3845	168	4224	614	11/12
52	29	209	31	306	2361	245	2439	614	10/12
18	12	227	31	359	1906	218	4233	620	10/11
17	12	239	32	386	3009	470	5599	624	9/11
19	12	269	31	378	3209	293	4849	633	8/9
Sample Sk3a (subhorizontal fabric)									
63	2	100	33	864	30214	601	32353	576	19/26
56	1	137	32	428	16927	28	8788	598	15/18
62	2	191	32	630	22249	163	11149	621	11/13
57	1	192	32	425	17057	5	8783	622	11/13
60	1	199	33	465	18779	48	9462	624	11/13
59	1	200	32	442	18663	98	9638	625	11/13
54	1	212	32	484	17913	42	9398	629	11/12
55	1	215	33	645	21962	104	11025	630	11/12
61	2	216	33	621	25687	48	13023	631	11/12
58	1	220	32	474	18557	21	9731	632	10/12
64	3	294	32	286	9263	148	5547	654	8/9
66	3	312	32	273	11185	131	6682	659	8/9
65	3	313	23	307	10452	126	6223	659	6/6
53	1	320	33	472	17762	72	9176	661	8/9

Crossed out values: discarded measurements due to high Si content (red), see text for explanation

Table S4. U-Pb LA-ICP-MS results for sample Sk3a (detrital zircon)

		Ratios								*Discordance*		*Ages*						
Name	$^{206}Pb_c$(%)*	206/204	$^{207}Pb/^{206}Pb^*$	1SE†	$^{207}Pb/^{235}U^*$	1SE	$^{206}Pb/^{238}U^*$	1SE	Rho§	Central (%)**	rim (%)	207/206	1s‡	207/235	1s‡	206/238	1s‡	
<5% Central Discordance																		
DG5_Sk3a_27	0.00E+00	11375	0.06458	0.00038	1.06318	0.01623	0.11940	0.00168	0.921	-4.7	-0.5	*761*	*12*	*735*	*8*	*727*	*10*	mixed age
DG5_Sk3a_53	0.00E+00	3022	0.06703	0.00043	1.26037	0.01837	0.13638	0.00179	0.900	-1.8	.	*839*	*13*	*828*	*8*	*824*	*10*	metamorphic?
DG5_Sk3a_79b	0.00E+00	2036	0.06995	0.00054	1.47258	0.02636	0.15267	0.00247	0.903	-1.3	.	927	15	919	11	916	14	
DG5_Sk3a_82	0.00E+00	3325	0.06998	0.00045	1.46824	0.01716	0.15216	0.00149	0.838	-1.7	.	928	13	917	7	913	8	
DG5_Sk3a_05	0.00E+00	477068	0.07060	0.00036	1.48942	0.01999	0.15301	0.00190	0.925	-3.2	-0.2	946	10	926	8	918	11	
DG5_Sk3a_71	0.00E+00	6116	0.07067	0.00048	1.51375	0.01695	0.15535	0.00139	0.797	-1.9	.	948	14	936	7	931	8	
DG5_Sk3a_25	0.00E+00	666024	0.07092	0.00041	1.49559	0.02172	0.15294	0.00204	0.919	-4.2	-0.9	955	11	929	9	917	11	
DG5_Sk3a_74	0.00E+00	1257	0.07127	0.00065	1.55441	0.02224	0.15818	0.00175	0.771	-2.1	.	965	18	952	9	947	10	
DG5_Sk3a_07	0.00E+00	6960	0.07147	0.00040	1.55646	0.02122	0.15795	0.00196	0.910	-2.8	.	971	12	953	8	945	11	
DG5_Sk3a_168	0.00E+00	4361	0.07156	0.00035	1.60921	0.02041	0.16309	0.00191	0.921	.	.	974	9	974	8	974	11	
DG5_Sk3a_26	0.00E+00	9360	0.07163	0.00041	1.58489	0.02346	0.16047	0.00219	0.922	-1.8	.	975	11	964	9	959	12	
DG5_Sk3a_66	0.00E+00	3339	0.07164	0.00047	1.61537	0.01882	0.16354	0.00158	0.829	0.1	.	976	13	976	7	976	9	
DG5_Sk3a_159	0.00E+00	1861	0.07170	0.00051	1.58137	0.02250	0.15997	0.00197	0.864	-2.3	.	977	14	963	9	957	11	
DG5_Sk3a_108	0.00E+00	2404	0.07193	0.00028	1.60216	0.01883	0.16155	0.00179	0.942	-2	.	984	8	971	7	965	10	
DG5_Sk3a_87	0.00E+00	4579	0.07194	0.00040	1.58561	0.01719	0.15985	0.00149	0.856	-3.1	-0.1	984	11	965	7	956	8	
DG_Sk3a_137	0.00E+00	17949	0.07222	0.00029	1.57654	0.01837	0.15832	0.00173	0.939	-4.8	-2.6	992	8	961	7	947	10	
DG_Sk3a_151	0.00E+00	3254	0.07244	0.00039	1.62657	0.02223	0.16285	0.00205	0.921	-2.8	.	998	11	981	9	973	11	
DG5_Sk3a_83	0.00E+00	7901	0.07286	0.00040	1.71970	0.01859	0.17117	0.00160	0.864	0.9	.	1010	11	1016	7	1019	9	
DG5_Sk3a_52	0.00E+00	9134	0.07298	0.00038	1.71402	0.01780	0.17035	0.00153	0.865	0.1	.	1013	10	1014	7	1014	8	
DG5_Sk3a_101	0.00E+00	2533	0.07304	0.00050	1.79516	0.02292	0.17824	0.00192	0.841	4.5	0.7	1015	14	1044	8	1057	10	
DG5_Sk3a_98	0.00E+00	3022	0.07305	0.00050	1.65468	0.01939	0.16427	0.00156	0.812	-3.7	-0.3	1015	13	991	7	980	9	
DG5_Sk3a_105	0.00E+00	7170	0.07311	0.00026	1.73796	0.01991	0.17241	0.00187	0.949	0.9	.	1017	7	1023	7	1025	10	
DG_Sk3a_142	0.00E+00	38968	0.07319	0.00025	1.73028	0.02016	0.17147	0.00191	0.956	0.1	.	1019	7	1020	7	1020	11	
DG5_Sk3a_121	0.00E+00	35768	0.07317	0.00026	1.71312	0.01942	0.16981	0.00183	0.949	-0.8	.	1019	7	1013	7	1011	10	
DG5_Sk3a_60	0.00E+00	1875	0.07341	0.00052	1.69017	0.01986	0.16699	0.00156	0.794	-3.1	.	1025	14	1005	7	995	9	
DG5_Sk3a_42	0.00E+00	11236	0.07343	0.00026	1.68312	0.02663	0.16624	0.00256	0.975	-3.6	-1.7	1026	7	1002	10	991	14	
DG5_Sk3a_91	0.00E+00	8088	0.07357	0.00041	1.76300	0.01896	0.17381	0.00160	0.855	0.4	.	1030	11	1032	7	1033	9	
DG5_Sk3a_77	0.00E+00	4214	0.07359	0.00047	1.72425	0.01879	0.16994	0.00151	0.813	-1.9	.	1030	12	1018	7	1012	8	
DG5_Sk3a_64	0.00E+00	6424	0.07361	0.00039	1.74054	0.01739	0.17149	0.00146	0.851	-1.1	.	1031	10	1024	6	1020	8	
DG5_Sk3a_131	0.00E+00	5895	0.07361	0.00028	1.72157	0.02016	0.16961	0.00188	0.946	-2.2	-0.1	1031	7	1017	8	1010	10	
DG5_Sk3a_115	0.00E+00	1225752	0.07398	0.00024	1.77774	0.02087	0.17427	0.00197	0.96	-0.6	.	1041	6	1037	8	1036	11	
DG5_Sk3a_161	0.00E+00	50210	0.07405	0.00026	1.74838	0.02130	0.17125	0.00200	0.959	-2.5	-0.5	1043	7	1027	8	1019	11	
DG5_Sk3a_94	0.00E+00	13134	0.07409	0.00040	1.79930	0.01908	0.17614	0.00161	0.864	0.2	.	1044	10	1045	7	1046	9	
DG5_Sk3a_128	0.00E+00	3579	0.07416	0.00033	1.80180	0.02224	0.17621	0.00203	0.931	.	.	1046	9	1046	8	1046	11	
DG5_Sk3a_04	0.00E+00	145033	0.07418	0.00043	1.78293	0.02483	0.17431	0.00220	0.907	-1.1	.	1046	12	1039	9	1036	12	
DG5_Sk3a_65	0.00E+00	6482	0.07438	0.00043	1.77588	0.01822	0.17316	0.00147	0.829	-2.3	.	1052	11	1037	7	1029	8	
DG5_Sk3a_156	0.00E+00	23190	0.07438	0.00027	1.77186	0.02264	0.17278	0.00212	0.959	-2.5	-0.5	1052	7	1035	8	1027	12	
DG5_Sk3a_81	0.00E+00	3254	0.07459	0.00047	1.77536	0.01943	0.17264	0.00155	0.819	-3.1	.	1057	12	1036	7	1027	9	
DG5_Sk3a_29	0.00E+00	11186	0.07464	0.00044	1.79409	0.02738	0.17434	0.00246	0.923	-2.3	.	1059	11	1043	10	1036	13	
DG5_Sk3a_176	0.00E+00	3755	0.07475	0.00032	1.83424	0.02378	0.17797	0.00217	0.942	-0.6	.	1062	8	1058	9	1056	12	
DG5_Sk3a_89	0.00E+00	10937	0.07475	0.00041	1.77636	0.01871	0.17236	0.00155	0.854	-3.7	-0.9	1062	11	1037	7	1025	9	
DG5_Sk3a_50	0.00E+00	6174	0.07481	0.00039	1.85315	0.01961	0.17966	0.00166	0.873	0.2	.	1063	10	1065	7	1065	9	
DG5_Sk3a_124	0.00E+00	3778	0.07496	0.00032	1.82091	0.02177	0.17618	0.00197	0.933	-2.2	.	1067	8	1053	8	1046	11	
DG5_Sk3a_90	0.00E+00	1216	0.07531	0.00054	1.82134	0.02216	0.17541	0.00172	0.806	-3.5	.	1077	14	1053	8	1042	9	
DG5_Sk3a_157	0.00E+00	2013	0.07559	0.00042	1.85819	0.02522	0.17828	0.00220	0.911	-2.7	.	1084	10	1066	9	1058	12	
DG5_Sk3a_164	0.00E+00	31443	0.07563	0.00030	1.91424	0.02369	0.18358	0.00215	0.946	0.1	.	1085	8	1086	8	1086	12	
DG5_Sk3a_111	0.00E+00	31623	0.07614	0.00029	1.88288	0.02357	0.17935	0.00214	0.954	-3.5	-1.5	1099	7	1075	8	1063	12	
DG5_Sk3a_126	0.00E+00	8929	0.07663	0.00029	1.94364	0.02381	0.18397	0.00214	0.950	-2.2	-0.2	1111	7	1096	8	1089	12	
DG5_Sk3a_99	0.00E+00	89199	0.07689	0.00042	1.99264	0.02477	0.18796	0.00209	0.896	-0.8	.	1118	11	1113	8	1110	11	
DG5_Sk3a_49	0.00E+00	4783	0.07691	0.00039	1.95836	0.02202	0.18468	0.00185	0.890	-2.6	.	1119	10	1101	8	1093	10	
DG5_Sk3a_88	0.00E+00	19811	0.07708	0.00041	1.98364	0.02142	0.18664	0.00175	0.870	-2	.	1123	10	1110	7	1103	10	
DG5_Sk3a_11	0.00E+00	4227	0.07723	0.00045	1.94815	0.02810	0.18296	0.00242	0.916	-4.2	-1.3	1127	11	1098	10	1083	13	

Mean = 937±14 [1.5%] 95% conf.
Wtd by data-pt errs only, 0 of 3 rej.
MSWD = 0.87, probability = 0.42

DG5_Sk3a_19_2	0.00E+00	32555	0.07749	0.00044	1.97609	0.02837	0.18496	0.00244	0.92	-3.8	-0.9	1134	11	1107	10	1094	13
DG5_Sk3a_84	0.00E+00	3794	0.07757	0.00048	1.96506	0.02436	0.18373	0.00198	0.867	-4.6	-1.7	1136	12	1104	8	1087	11
DG5_Sk3a_19_1	0.00E+00	10044	0.07785	0.00047	1.99217	0.02916	0.18560	0.00248	0.912	-4.3	-1.3	1143	11	1113	10	1098	13
DG5_Sk3a_85	0.00E+00	2686	0.07789	0.00050	2.07672	0.02292	0.19337	0.00174	0.813	-0.4	.	1144	12	1141	8	1140	9
DG5_Sk3a_109	0.00E+00	26353	0.07955	0.00027	2.26728	0.02732	0.20671	0.00239	0.959	2.3	.	1186	6	1202	8	1211	13
DG5_Sk3a_62	0.00E+00	12758	0.08346	0.00045	2.46554	0.02660	0.21426	0.00200	0.864	-2.4	.	1280	10	1262	8	1251	11
DG5_Sk3a_118	0.00E+00	18164	0.08514	0.00030	2.60980	0.03171	0.22231	0.00259	0.958	-2.1	-0.4	1319	7	1303	9	1294	14
DG_Sk3a_133	0.00E+00	12114	0.08565	0.00034	2.66907	0.03425	0.22602	0.00275	0.95	-1.4	.	1330	8	1320	9	1314	14
DG_Sk3a_140	0.00E+00	108421	0.08594	0.00030	2.71705	0.03431	0.22931	0.00278	0.961	-0.5	.	1337	6	1333	9	1331	15
DG5_Sk3a_72	0.00E+00	3484	0.08725	0.00053	2.74551	0.03023	0.22821	0.00210	0.834	-3.3	-0.8	1366	12	1341	8	1325	11
DG5_Sk3a_162	0.00E+00	16608	0.08736	0.00036	2.81663	0.03725	0.23385	0.00294	0.951	-1.1	.	1368	8	1360	10	1355	15
DG_Sk3a_139	0.00E+00	11283	0.08805	0.00036	2.84328	0.03692	0.23419	0.00289	0.949	-2.2	-0.3	1384	8	1367	10	1356	15
DG5_Sk3a_166	0.00E+00	10385	0.08811	0.00035	2.86556	0.03840	0.23588	0.00302	0.954	-1.6	.	1385	7	1373	10	1365	16
DG5_Sk3a_125	0.00E+00	9126	0.08825	0.00033	2.86494	0.03610	0.23544	0.00283	0.955	-2	-0.3	1388	7	1373	9	1363	15
DG_Sk3a_135	0.00E+00	3346	0.08989	0.00037	2.97612	0.03853	0.24014	0.00295	0.947	-2.8	-1	1423	8	1402	10	1387	15
DG5_Sk3a_48	0.00E+00	16951	0.09010	0.00053	3.04405	0.03575	0.24502	0.00249	0.864	-1.2	.	1428	11	1419	9	1413	13
DG_Sk3a_147	0.00E+00	49727	0.09072	0.00038	3.05235	0.04206	0.24402	0.00321	0.954	-2.6	-0.7	1441	8	1421	11	1408	17
DG5_Sk3a_43	0.00E+00	60740	0.09103	0.00020	3.08295	0.05017	0.24562	0.00396	0.991	-2.4	-1.5	1447	4	1428	12	1416	20
DG5_Sk3a_54	0.00E+00	29553	0.09123	0.00058	3.08624	0.05520	0.24534	0.00410	0.934	-2.8	-0.1	1451	12	1429	14	1414	21
DG5_Sk3a_56	0.00E+00	31432	0.09127	0.00049	3.02587	0.03297	0.24045	0.00228	0.87	-4.8	-2.7	1452	10	1414	8	1389	12
DG5_Sk3a_97	0.00E+00	21484	0.09150	0.00051	3.20685	0.03953	0.25419	0.00280	0.893	0.2	.	1457	10	1459	10	1460	14
DG5_Sk3a_80	0.00E+00	19172	0.09279	0.00052	3.28086	0.03658	0.25643	0.00248	0.866	-0.9	.	1484	10	1477	9	1472	13
DG5_Sk3a_110	0.00E+00	54374	0.09295	0.00033	3.28508	0.04436	0.25634	0.00334	0.966	-1.2	.	1487	6	1478	11	1471	17
DG5_Sk3a_127	0.00E+00	39361	0.09337	0.00033	3.30276	0.04308	0.25655	0.00322	0.964	-1.7	-0.2	1495	6	1482	10	1472	17
DG5_Sk3a_57	0.00E+00	10760	0.09364	0.00055	3.23714	0.03645	0.25073	0.00241	0.854	-4.4	-2.1	1501	11	1466	9	1442	12
DG5_Sk3a_100	0.00E+00	26899	0.09444	0.00054	3.37384	0.03946	0.25909	0.00265	0.874	-2.3	.	1517	10	1498	9	1485	14
DG5_Sk3a_155	0.00E+00	58042	0.09498	0.00036	3.33899	0.05343	0.25496	0.00396	0.972	-4.7	-3.1	1528	7	1490	13	1464	20
DG5_Sk3a_106	0.00E+00	8277	0.09625	0.00037	3.54606	0.04673	0.26722	0.00337	0.956	-1.9	-0.2	1553	7	1538	10	1527	17
DG5_Sk3a_163	0.00E+00	8217	0.09860	0.00040	3.65624	0.05016	0.26895	0.00352	0.955	-4.4	-2.7	1598	7	1562	11	1535	18
DG5_Sk3a_116	0.00E+00	56187	0.09940	0.00039	3.72652	0.05239	0.27189	0.00367	0.96	-4.4	-2.8	1613	7	1577	11	1550	19
DG5_Sk3a_86	0.00E+00	8764	0.10002	0.00060	3.87923	0.04850	0.28130	0.00309	0.878	-1.8	.	1624	11	1609	10	1598	16
DG5_Sk3a_24	0.00E+00	14072	0.10055	0.00063	3.82849	0.06428	0.27616	0.00430	0.927	-4.3	-1.8	1634	11	1599	14	1572	22
DG5_Sk3a_35	0.00E+00	275503	0.10119	0.00020	3.93716	0.05426	0.28218	0.00385	0.989	-3	-2.3	1646	4	1621	11	1602	19
DG5_Sk3a_15	0.00E+00	4930	0.10151	0.00080	3.96951	0.07264	0.28363	0.00469	0.903	-2.9	.	1652	14	1628	15	1610	24
DG5_Sk3a_75	0.00E+00	33587	0.10159	0.00057	3.92545	0.04497	0.28023	0.00281	0.874	-4.2	-2.1	1653	10	1619	9	1593	14
DG5_Sk3a_18	0.00E+00	280080	0.10468	0.00065	4.27599	0.07118	0.29627	0.00458	0.928	-2.4	.	1709	11	1689	14	1673	23
DG5_Sk3a_40	0.00E+00	230549	0.10578	0.00022	4.29465	0.06532	0.29447	0.00444	0.99	-4.2	-3.5	1728	4	1692	13	1664	22
DG5_Sk3a_169	0.00E+00	29520	0.10618	0.00044	4.42098	0.06450	0.30197	0.00423	0.960	-2.2	-0.6	1735	7	1716	12	1701	21
DG5_Sk3a_114	0.00E+00	33023	0.11170	0.00043	5.03480	0.07473	0.32691	0.00469	0.966	-0.2	.	1827	7	1825	13	1823	23
>5% Central Discordance																	
DG5_Sk3a_08	0.00E+00	4047	0.07212	0.00042	1.56540	0.02159	0.15742	0.00197	0.906	-5.1	-1.9	989	12	957	9	942	11
DG5_Sk3a_30	0.00E+00	4323	0.08388	0.00060	2.43058	0.03991	0.21017	0.00310	0.900	-5.1	-1.9	1290	14	1252	12	1230	17
DG5_Sk3a_104	0.00E+00	15584	0.08811	0.00042	2.75898	0.03871	0.22711	0.00299	0.940	-5.2	-3.1	1385	9	1345	10	1319	16
DG_Sk3a_149	0.00E+00	7844	0.07843	0.00033	2.01486	0.02449	0.18631	0.00213	0.940	-5.3	-3.2	1158	8	1121	8	1101	12
DG5_Sk3a_10	0.00E+00	10038	0.08155	0.00046	2.24720	0.03213	0.19985	0.00262	0.918	-5.3	-2.7	1235	10	1196	10	1175	14
DG5_Sk3a_70	0.00E+00	6229	0.08689	0.00056	2.65984	0.03119	0.22202	0.00217	0.834	-5.3	-2.7	1358	12	1317	9	1293	11
DG5_Sk3a_39	0.00E+00	12637	0.08696	0.00022	2.66092	0.03966	0.22192	0.00326	0.986	-5.5	-4.4	1360	5	1318	11	1292	17
DG5_Sk3a_68	0.00E+00	28496	0.07183	0.00037	1.53757	0.01575	0.15525	0.00137	0.864	-5.6	-2.8	981	10	946	6	930	8
DG5_Sk3a_61	0.00E+00	36656	0.07372	0.00039	1.66833	0.01676	0.16413	0.00140	0.849	-5.6	-3	1034	11	997	6	980	8
DG5_Sk3a_59	0.00E+00	3157	0.07409	0.00043	1.69482	0.01808	0.16591	0.00148	0.838	-5.6	-2.7	1044	11	1007	7	990	8
DG5_Sk3a_06	0.00E+00	14091	0.07442	0.00045	1.71819	0.03081	0.16745	0.00283	0.941	-5.6	-2.4	1053	12	1015	12	998	16
DG_Sk3a_144	0.00E+00	4773	0.07339	0.00039	1.64437	0.02242	0.16251	0.00204	0.919	-5.7	-2.8	1025	10	987	9	971	11
DG_Sk3a_153	0.00E+00	20990	0.09878	0.00039	3.62024	0.05024	0.26581	0.00354	0.959	-5.7	-4.2	1601	7	1554	11	1520	18
DG5_Sk3a_112	0.00E+00	20402	0.10094	0.00039	3.79631	0.05359	0.27277	0.00370	0.961	-5.9	-4.4	1641	7	1592	11	1555	19
DG5_Sk3a_33	0.00E+00	30280	0.07310	0.00017	1.61854	0.02165	0.16059	0.00212	0.985	-6	-4.8	1017	4	977	8	960	12
DG5_Sk3a_44	0.00E+00	6772	0.06549	0.00030	1.10598	0.01929	0.12248	0.00206	0.965	-6.1	-2.9	790	10	756	9	745	12

DG5_Sk3a_37	0.00E+00	22019	0.09197	0.00025	3.04335	0.04443	0.23999	0.00344	0.982	-6.1	-5	1467	5	1419	11	1387	18
DG5_Sk3a_76	0.00E+00	1852	0.08580	0.00059	2.54983	0.03060	0.21554	0.00211	0.816	-6.2	-3.4	1334	13	1286	9	1258	11
DG5_Sk3a_09	0.00E+00	16697	0.09124	0.00052	2.97814	0.04466	0.23673	0.00328	0.925	-6.3	-3.9	1452	10	1402	11	1370	17
DG5_Sk3a_20	0.00E+00	31535	0.09226	0.00054	3.05913	0.04932	0.24049	0.00361	0.931	-6.3	-3.9	1473	11	1423	12	1389	19
DG5_Sk3a_32	0.00E+00	45064	0.09489	0.00019	3.27088	0.04540	0.25001	0.00343	0.989	-6.4	-5.6	1526	4	1474	11	1439	18
DG5_Sk3a_96	0.00E+00	6725	0.17219	0.00135	10.92427	0.17512	0.46014	0.00643	0.871	-6.5	-4.2	2579	12	2517	15	2440	28
DG5_Sk3a_41	0.00E+00	39192	0.10122	0.00021	3.78466	0.05760	0.27119	0.00409	0.99	-6.8	-6.1	1647	4	1589	12	1547	21
DG5_Sk3a_175	0.00E+00	2258306289	0.11705	0.00052	5.17883	0.08042	0.32090	0.00478	0.958	-7	-5.5	1912	8	1849	13	1794	23
DG5_Sk3a_119	0.00E+00	4111	0.07844	0.00060	1.97776	0.03224	0.18286	0.00263	0.884	-7.1	-3.5	1158	15	1108	11	1083	14
DG_Sk3a_136	0.00E+00	9782	0.08330	0.00034	2.33419	0.03070	0.20323	0.00254	0.952	-7.2	-5.3	1276	8	1223	9	1193	14
DG5_Sk3a_51	0.00E+00	6926	0.09269	0.00056	3.06081	0.04395	0.23950	0.00312	0.908	-7.3	-4.9	1482	11	1423	11	1384	16
DG_Sk3a_141	0.00E+00	12110	0.11010	0.00046	4.53645	0.06674	0.29883	0.00421	0.958	-7.3	-5.8	1801	7	1738	12	1686	21
DG5_Sk3a_129	0.00E+00	7069	0.07609	0.00050	1.80006	0.02314	0.17158	0.00189	0.859	-7.5	-4.4	1097	13	1045	8	1021	10
DG5_Sk3a_93	0.00E+00	10594	0.08504	0.00049	2.45110	0.02832	0.20906	0.00209	0.864	-7.7	-5.3	1316	11	1258	8	1224	11
DG5_Sk3a_55	0.00E+00	18377	0.07896	0.00076	1.99718	0.03055	0.18345	0.00217	0.775	-7.9	-3.8	1171	18	1115	10	1086	12
DG5_Sk3a_160	0.00E+00	35634	0.08997	0.00039	2.82403	0.04124	0.22765	0.00317	0.954	-8	-6.1	1425	8	1362	11	1322	17
DG5_Sk3a_107	0.00E+00	19118	0.08995	0.00033	2.81035	0.03562	0.22659	0.00275	0.958	-8.4	-6.9	1425	7	1358	9	1317	14
DG5_Sk3a_92	0.00E+00	31626	0.17968	0.00142	11.53935	0.17817	0.46578	0.00617	0.858	-8.4	-6.3	2650	13	2568	14	2465	27
DG5_Sk3a_45	0.00E+00	2751	0.09842	0.00054	3.47441	0.06590	0.25604	0.00465	0.957	-8.8	-6.6	1594	10	1521	15	1470	24
DG5_Sk3a_103	0.00E+00	4808	0.08163	0.00047	2.16649	0.02417	0.19249	0.00185	0.859	-9	-6.5	1237	11	1170	8	1135	10
DG5_Sk3a_170	0.00E+00	11799	0.09910	0.00053	3.51829	0.06826	0.25748	0.00481	0.962	-9.1	-7.1	1607	10	1531	15	1477	25
DG5_Sk3a_172	0.00E+00	17713	0.08425	0.00133	2.34814	0.06653	0.20214	0.00476	0.831	-9.4	-2.9	1298	30	1227	20	1187	26
DG5_Sk3a_165	0.00E+00	40765	0.07674	0.00028	1.80759	0.02231	0.17083	0.00201	0.954	-9.5	-7.7	1115	7	1048	8	1017	11
DG5_Sk3a_174	0.00E+00	24205	0.10306	0.00042	3.82098	0.05493	0.26890	0.00370	0.958	-9.7	-8.2	1680	7	1597	12	1535	19
DG5_Sk3a_154	0.00E+00	24847	0.10346	0.00041	3.84261	0.05613	0.26936	0.00378	0.962	-10	-8.5	1687	7	1602	12	1538	19
DG5_Sk3a_79	0.00E+00	9900	0.06842	0.00037	1.24236	0.01438	0.13170	0.00135	0.887	-10.1	-7.1	881	11	820	7	798	8
DG5_Sk3a_22	0.00E+00	24700	0.09075	0.00058	2.81288	0.05049	0.22480	0.00377	0.934	-10.3	-7.7	1441	12	1359	13	1307	20
DG5_Sk3a_130	0.00E+00	20420	0.09775	0.00037	3.32668	0.04892	0.24683	0.00351	0.967	-11.2	-9.8	1582	7	1487	11	1422	18
DG5_Sk3a_16	0.00E+00	145524	0.09890	0.00061	3.41042	0.05626	0.25009	0.00383	0.928	-11.4	-9.2	1604	11	1507	13	1439	20
DG5_Sk3a_171	0.00E+00	22302	0.09347	0.00036	2.98107	0.04119	0.23131	0.00307	0.960	-11.5	-10	1497	7	1403	11	1341	16
DG5_Sk3a_47	0.00E+00	10382	0.08802	0.00052	2.54651	0.02966	0.20983	0.00211	0.861	-12.3	-10	1383	11	1285	8	1228	11
DG5_Sk3a_23	0.00E+00	7975	0.08764	0.00054	2.51383	0.04074	0.20804	0.00312	0.926	-12.5	-10	1375	11	1276	12	1218	17
DG5_Sk3a_69	0.00E+00	23702	0.08675	0.00053	2.40442	0.03730	0.20103	0.00287	0.919	-14.1	-11.6	1355	12	1244	11	1181	15
DG5_Sk3a_03	0.00E+00	75131	0.09559	0.00061	3.03438	0.05032	0.23023	0.00353	0.924	-14.7	-12.4	1540	12	1416	13	1336	18
DG_Sk3a_152	0.00E+00	2083	0.07199	0.00058	1.39136	0.03513	0.14017	0.00335	0.947	-15.2	-11	986	16	885	15	846	19
DG_Sk3a_145	0.00E+00	27182	0.08246	0.00029	2.03917	0.02476	0.17935	0.00209	0.958	-16.7	-15.2	1256	7	1129	8	1063	11
DG5_Sk3a_102	0.00E+00	5395	0.06770	0.00040	1.10330	0.01445	0.11820	0.00138	0.890	-17.1	-13.9	859	12	755	7	720	8
DG5_Sk3a_36	0.00E+00	34536	0.08351	0.00037	2.08783	0.03610	0.18133	0.00303	0.966	-17.5	-15.7	1281	8	1145	12	1074	17
DG5_Sk3a_95	0.00E+00	26642	0.09474	0.00059	2.87051	0.04211	0.21974	0.00292	0.906	-17.5	-15.4	1523	11	1374	11	1281	15
DG_Sk3a_134	0.00E+00	28096	0.10595	0.00040	3.71355	0.04952	0.25420	0.00325	0.959	-17.5	-16.2	1731	7	1574	11	1460	17
DG5_Sk3a_167	0.00E+00	139684	0.08215	0.00032	1.94087	0.02505	0.17135	0.00211	0.953	-19.9	-18.3	1249	7	1095	9	1020	12
DG5_Sk3a_12	0.00E+00	17994	0.08977	0.00059	2.25255	0.03628	0.18199	0.00267	0.912	-26.2	-24	1421	12	1198	11	1078	15
DG5_Sk3a_73	0.00E+00	26725	0.09823	0.00074	2.67490	0.04493	0.19749	0.00296	0.892	-29.4	-27.3	1591	14	1322	12	1162	16
DG5_Sk3a_113	0.00E+00	4175	0.10363	0.00425	2.69796	0.11709	0.18883	0.00268	0.327	-37	-28.2	1690	74	1328	32	1115	15
DG5_Sk3a_28	0.00E+00	56108	0.12653	0.00166	3.22069	0.07809	0.18460	0.00376	0.84	-50.7	-48.5	2050	22	1462	19	1092	20
DG5_Sk3a_120	0.00E+00	11402	0.54977	0.45381	23.90157	20.28942	0.31532	0.06242	0.233	-67.6	.	4381	3223	3264	827	1767	306

*applied common Pb correction in % (counts on 204 did not exceed background level for any of the analyses)

** Central discordance corresponds to the distance between the center of the error ellipse and the Concordia curve.

† 1 SE corresponds to the error on the raw data

‡ 1 s corresponds to the error on the age calculation including the errors on the raw data, the standard curve and the standard values

§ rho corresponds to the error correlation

Table S5. SIMS U-Th-Pb zircon data for leucosome sample Sk3c

							TW Concordia columns (Pbc corrected)				Ages			
Sample/	**[U]**	**[Th]**	**[Pb]**	**Th/U**	**f_{206}%**	**$^{206}Pb/^{204}Pb$**	**$^{238}U/^{206}Pb$**	**±σ**	**$^{207}Pb/^{206}Pb$**	**±σ**	**$^{207}Pb/^{206}Pb$**	**±σ**	**$^{206}Pb/^{238}U$**	**±σ**
spot #	**ppm**	**ppm**	**ppm**	**calc**		**measured**		**%**		**%**				
n4288-b12	1885.8	3.1	[238]	no data	9.52	196	9.2442	0.87	0.06540	10.18	650	23	710	6
n4288-b16	1862.7	4.6	225.8	0.00	0.04	47817	8.7889	0.90	0.06301	0.83	670	11	696	6
n4288-b4	1056.8	4.0	[131]	no data	0.02	96598	8.7742	0.72	0.06259	0.38	677	15	708	6
n4288_16	1452.7	4.6	[188]	no data	{0.00}	380167	8.7660	0.90	0.06187	0.52	685	21	720	4
n4288-b07	1391.4	4.2	177.4	0.00	{0.01}	247438	8.6170	1.05	0.06329	0.41	690	12	730	8
n4288_19	1436.2	4.2	181.0	0.00	0.48	3886	8.6188	0.88	0.06208	0.72	691	6	722	4
n4288-b08	1477.5	4.4	185.6	0.00	1.19	1578	8.5874	0.87	0.06129	1.09	693	8	720	6
n4288_03	820.2	3.6	99.4	0.00	0.02	101218	8.5679	0.97	0.06284	0.46	694	8	696	5
n4288_07	1467.5	3.9	184.1	0.00	{0.00}	735550	8.5578	0.62	0.06302	0.29	695	7	719	4
n4288-b13	1199.2	3.4	151.9	0.00	{0.01}	348693	8.5090	0.97	0.06315	0.39	697	9	726	6
n4288-b10	1716.5	4.0	218.0	0.00	{0.01}	262589	8.4837	0.91	0.06281	0.38	699	10	727	6
n4288-b02	1545.6	4.6	197.0	0.00	0.01	194203	8.4774	0.64	0.06260	0.33	701	9	730	6
n4288_05	1327.3	4.0	167.9	0.00	0.01	326485	8.4658	0.61	0.06281	0.29	701	6	724	4
n4288-b04 - spot2	1410.6	3.9	176.9	0.00	{0.01}	357881	8.4645	0.90	0.06256	0.39	702	8	718	6
n4288_09	1599.7	3.9	201.0	0.00	1.96	952	8.4670	0.64	0.06231	0.97	702	6	720	4
n4288-b17	1584.2	4.6	196.6	0.00	{0.01}	312934	8.4575	0.65	0.06316	0.29	703	10	712	7
n4288_13	1393.7	4.2	177.1	0.00	0.03	58450	8.4345	0.61	0.06250	0.30	705	9	728	4
n4288-b15	868.1	5.2	105.2	0.01	0.03	59518	8.4094	0.65	0.06279	0.30	709	18	695	6
n4288_17	1391.8	3.7	173.0	0.00	{0.00}	493443	8.3980	0.90	0.06337	0.42	709	6	712	4
n4288-b05	2325.4	7.2	296.4	0.00	0.01	154401	8.3970	0.64	0.06310	0.52	710	8	729	6
n4288_10	956.1	3.2	121.1	0.00	{0.00}	579741	8.3938	0.91	0.06266	0.41	712	11	725	4
n4288-b14	1350.6	3.9	168.9	0.00	{0.01}	275715	8.3752	0.88	0.06272	0.46	713	8	716	7
n4288_1	1335.2	5.0	168.0	0.00	0.01	139187	8.3701	0.62	0.06290	0.42	714	6	720	4
n4288-b03	1604.5	3.7	198.1	0.00	{0.00}	659614	8.3491	0.88	0.06305	0.37	718	9	708	7
n4288_02	1108.8	4.3	141.6	0.01	0.22	8383	8.3381	0.68	0.06333	0.62	719	13	730	5
n4288-b20	1624.2	6.2	205.9	0.00	{0.01}	252304	8.3436	0.92	0.06278	0.43	721	9	725	6
n4288_20	1166.2	35.2	153.0	0.04	0.12	15535	8.3396	1.18	0.06247	0.58	758	7	741	5
n4288_06	955.6	3.7	135.9	0.00	0.01	134483	8.2064	0.66	0.06450	0.31	768	45	807	8
n4288-b19	1322.9	4.4	153.4	0.02	17.00	110	7.9759	0.58	0.06978	8.61	787	200	662	5
n4288_18	639.0	56.3	94.3	0.11	14.47	129	7.6224	0.65	0.06881	10.70	826	8	811	5
n4288-b11	248.4	44.0	38.7	0.19	1.51	1235	7.4944	1.11	0.06482	2.17	855	28	836	8
n4288_14	2647.6	461.4	388.1	0.14	0.06	31862	7.4590	0.67	0.06661	0.41	893	207	795	5
n4288_15	1010.3	31.2	264.6	0.01	3.92	477	7.2564	0.61	0.07826	1.11	905	41	1410	7
n4288_12	430.5	23.2	59.1	0.07	1.08	1727	7.2204	1.08	0.06755	1.35	922	168	761	4
n4288_11	850.2	1099.3	199.5	1.38	0.02	90653	6.3482	0.91	0.07585	0.45	953	7	941	5
n4288-b18	368.2	138.7	75.9	0.38	{0.00}	413708	6.3636	0.58	0.07084	0.32	1028	13	1033	8
n4288-b06	668.2	365.9	133.7	0.55	{0.02}	107278	5.7553	0.87	0.07350	0.66	1091	9	943	8
n4288-b1	185.9	78.8	40.7	0.42	{0.03}	72557	5.5040	0.90	0.07669	0.79	1113	16	1076	9
n4288_08	686.8	308.3	118.6	0.41	0.02	115440	3.7739	1.45	0.11131	0.47	1154	22	832	5
n4288_04	706.8	338.8	239.8	0.48	11.62	161	4.0906	0.58	0.06922	2.03	1821	8	1515	20

Table S6. Representative monazite EMP analyses

Spot	P_2O_5	ThO_2	Y_2O_3	Ce_2O_3	La_2O_3	Pr_2O_3	Nd_2O_3	CaO	SiO_2	Sm_2O_3	Gd_2O_3	UO_3	Total	dated *
sample Sk3c, leucosome														
8	30.96	3.76	3.54	26.54	12.35	3.12	11.83	1.13	0.10	2.76	2.13	1.62	99.84	11
16	31.23	3.39	3.15	27.59	13.54	3.04	11.55	1.05	0.07	2.56	1.71	1.62	100.49	14
15	31.18	3.88	3.32	26.84	12.90	3.00	11.56	1.20	0.10	2.56	1.78	1.84	100.17	20
6	31.21	3.99	3.46	26.61	12.30	2.99	11.85	1.20	0.08	2.80	2.07	1.71	100.25	6
14	31.18	4.13	3.31	26.60	12.72	3.04	11.50	1.23	0.10	2.66	1.92	1.73	100.13	25
5	30.96	4.25	2.90	26.65	13.24	3.05	11.12	1.36	0.16	2.58	1.63	2.37	100.28	2
4	31.14	3.83	3.18	26.92	12.63	3.10	11.82	1.14	0.08	2.83	1.81	1.56	100.03	1
7	31.35	3.58	3.25	27.27	12.41	3.05	12.03	1.04	0.10	2.88	1.98	1.50	100.46	8
9	30.95	3.60	2.87	27.71	13.01	3.22	12.09	1.01	0.12	2.58	1.73	1.18	100.08	-
10	31.00	3.89	3.08	27.22	12.78	3.14	11.89	1.08	0.13	2.65	1.80	1.31	99.97	-
11	31.20	3.93	2.90	27.89	13.34	3.01	11.81	0.99	0.11	2.79	1.70	0.91	100.56	-
12	31.09	3.60	3.04	27.33	12.69	3.11	12.23	1.02	0.08	2.82	1.96	1.19	100.17	-
13	30.88	3.41	2.59	27.68	13.16	3.27	12.11	1.04	0.11	2.79	1.65	1.77	100.45	-
sample Sk3d, melanosome														
33	31.10	3.71	2.82	27.52	13.15	3.08	11.93	1.05	0.07	2.79	1.87	1.25	100.34	61
36	30.72	3.52	2.41	27.93	13.47	3.13	12.19	1.00	0.07	2.72	1.70	1.16	100.02	71
22	30.91	3.97	2.41	27.60	13.22	3.08	11.88	1.11	0.08	2.62	1.82	1.29	99.99	12a_rim
20	30.99	3.62	3.05	27.71	13.04	3.14	12.28	0.92	0.08	2.79	1.93	0.84	100.41	9b_core
18	31.19	3.38	3.10	27.28	13.22	3.05	11.52	1.13	0.09	2.48	1.70	1.97	100.11	2
29	31.02	3.86	2.24	28.09	13.28	3.13	12.04	1.07	0.11	2.68	1.79	1.23	100.56	37a_rim
32	31.16	3.37	3.23	27.36	12.90	3.08	12.09	1.00	0.07	2.77	1.82	1.26	100.11	50
17	30.87	3.53	2.89	27.47	13.21	3.04	12.04	1.01	0.11	2.59	1.89	1.18	99.83	1
31	31.13	3.77	2.87	27.04	12.96	3.12	12.26	1.09	0.10	2.73	1.88	1.27	100.22	49
30	29.46	6.85	2.11	28.79	11.17	3.30	12.52	0.72	1.03	2.78	1.61	0.13	100.47	37b_core
35	29.88	4.31	2.47	28.05	13.53	3.16	12.79	0.48	0.65	2.47	1.68	0.34	99.81	67a_core
19	31.17	3.73	3.12	26.93	13.19	3.10	12.05	1.05	0.09	2.76	1.96	1.24	100.40	9a_rim
34	31.10	1.44	2.92	28.89	14.09	3.18	12.13	0.60	0.04	2.90	1.89	1.08	100.27	67b_rim
24	31.00	3.79	3.37	27.24	12.93	3.07	11.90	1.08	0.08	2.68	1.79	1.38	100.31	-
25	31.33	3.63	2.93	27.29	13.26	3.17	12.12	1.07	0.07	2.73	1.94	1.17	100.70	-
26	31.44	3.55	3.31	27.09	13.17	3.06	12.11	1.00	0.09	2.71	2.10	1.00	100.61	-
27	31.04	3.66	3.38	27.15	12.73	3.05	12.04	1.05	0.08	2.64	2.06	1.29	100.18	-
28	31.09	3.70	2.23	28.04	13.28	3.33	12.13	1.02	0.08	2.78	1.83	1.21	100.72	-
21	30.83	3.59	3.00	27.32	12.99	3.05	12.09	1.00	0.07	2.68	2.02	1.05	99.71	-

* The spot number of U-Pb-Th SIMS analyses is given, which can be found in table S7. The analyses are sorted from old to young.

Table S7. SIMS U-Th-Pb monazite data for leucosome sample Sk3c and melanosome sample Sk3d

							TW Concordia columns (Pbc corrected)				Ages			
Sample/ spot #	**[U] ppm**	**[Th] ppm**	**[Pb] ppm**	**Th/U calc**	**f_{206}%**	**$^{206}Pb/^{204}Pb$ measured**	**$^{238}U/^{206}Pb$**	**±σ %**	**$^{207}Pb/^{206}Pb$**	**±σ %**	**$^{207}Pb/^{206}Pb$**	**±σ**	**$^{206}Pb/^{238}U$**	**±σ**
sample Sk3c, leucosome														
n4465_(1094)_11	13013	27628	2636	2.12	0.01	305324	8.3981	3.24	0.06306	0.44	710	9	725	22
n4465_(1093)_14	14101	33056	3012	2.45	0.01	126539	8.4426	3.54	0.06304	0.47	710	10	722	24
n4465_(1093)_20	14545	35873	3054	2.46	0.01	210921	8.6007	3.35	0.06271	0.43	699	9	709	23
n4465_(1094)_6	11896	31325	2592	2.76	{0.01}	276577	8.7545	3.36	0.06261	0.55	695	12	697	22
n4465_(1093)_25	12604	31288	2671	2.52	0.02	111434	8.4918	3.54	0.06231	0.44	685	9	718	24
n4465_(1094)_10	18641	32073	3449	1.84	0.01	282004	8.6451	3.40	0.06192	0.48	672	10	706	23
n4465_(1094)_5	14572	35066	3114	2.62	0.01	209848	8.4736	3.40	0.06191	0.46	671	10	719	23
n4465_(1094)_2	21894	35656	3847	1.78	0.02	78189	8.9583	3.38	0.06103	0.42	640	9	682	22
n4465_(1094)_1	11167	29832	2159	2.74	0.01	138684	9.8986	3.28	0.06062	0.53	626	11	620	19
n4465_(1094)_8	11236	32054	2238	2.96	{0.01}	209253	9.7723	3.33	0.06016	0.56	609	12	628	20
sample Sk3d, melanosome														
n4466_(1094)_12b (core)	7656	50778	3698	8.46	0.03	69009	7.2239	3.38	0.06537	0.59	786	12	836	27
n4466_(1094)_35	9335	30679	2481	3.48	0.02	75777	7.9300	3.47	0.06429	0.57	751	12	766	25
n4466_(1094)_61	8660	29999	2256	3.44	0.02	116010	8.1287	3.38	0.06415	0.53	747	11	748	24
n4466_(1094)_64	9830	30045	2438	3.07	0.02	111922	8.0012	3.38	0.06406	0.53	744	11	759	24
n4466_(1094)_71	9780	34074	2577	3.53	0.01	176356	8.0684	3.33	0.06395	0.54	740	11	753	24
n4466_(1094)_12a (rim)	9637	33385	2452	3.39	0.01	141275	8.2432	3.43	0.06378	0.51	734	11	738	24
n4466_(1094)_9b (core)	5777	39185	2371	7.45	0.03	59775	7.8428	3.24	0.06372	0.64	732	13	774	24
n4466_(1094)_55	10292	36901	2730	3.65	0.02	108256	8.0615	3.46	0.06350	0.51	725	11	754	25
n4466_(1094)_2	16485	31376	3163	1.84	{0.00}	>1e6	8.4979	3.28	0.06337	0.38	721	8	717	22
n4466_(1094)_37a (rim)	9704	33102	2455	3.43	0.01	353021	8.2290	3.30	0.06324	0.55	716	12	739	23
n4466_(1094)_50	9399	31245	2325	3.35	0.02	112613	8.4049	3.40	0.06322	0.51	716	11	725	23
n4466_(1094)_1	7763	30111	2090	4.07	0.02	85784	8.5538	3.36	0.06298	0.59	708	12	713	23
n4466_(1094)_49	7720	33848	2187	4.41	0.01	287798	8.4036	3.54	0.06294	0.63	706	13	725	24
n4466_(1094)_37b (core)	4357	39384	2270	11.56	0.03	62122	9.3847	3.12	0.06278	1.07	701	23	653	19
n4466_(1094)_66	9731	30332	2375	3.42	0.01	185124	8.5144	3.15	0.06256	0.51	693	11	716	21
n4466_(1094)_63	9732	31912	2293	3.37	0.01	208043	8.7819	3.50	0.06206	0.53	676	11	695	23
n4466_(1094)_70	8945	31237	2047	3.64	0.01	159154	9.4365	3.43	0.06089	0.56	635	12	649	21
n4466_(1094)_67a (core)	7057	14874	1204	2.02	{0.00}	>1e6	9.8192	3.04	0.06041	0.68	618	15	625	18
n4466_(1094)_9a (rim)	5500	30448	1582	5.70	0.04	45964	9.5542	3.57	0.06037	0.75	617	16	642	22
n4466_(1094)_67b (rim)	7391	14803	1240	2.10	0.02	75982	10.0850	2.89	0.05973	0.84	594	18	609	17

Table S8. U-Pb TIMS data for rutile and titanite

Nr.	Properties	Weight [μg] (1)	U [ppm] (1)	Th/U (3)	Pbc [ppm] (1,2)	Pbcom [pg] (4)	$^{206}Pb/^{204}Pb$ (5)	$^{207}Pb/^{235}U$ (6)	2σ [abs] (6)	$^{206}Pb/^{238}Pb$ (6)	2σ [abs] (6)	ρ (6)	$^{206}Pb/^{238}U$ [Ma] (6)	2σ [Ma] (6)	$^{207}Pb/^{235}U$ [Ma] (6)	2σ [Ma] (6)
Rutiles																
sample Sk3d, melanosome subvertical fabric																
338/15	longprismatic, olive	2	52	---	3.58	9.1	68	0.358	0.039	0.0689	0.0005	0.77	429.5	2.8	310	29
338/16	irregular, reddish	9	27	---	0.81	9.3	129	0.424	0.023	0.0679	0.0006	0.46	423.5	3.9	359	16
338/21	round, metallic green	41	16	0.03	0.19	9.9	304	0.483	0.015	0.0671	0.0012	0.57	418.9	7.4	400	10
347/19	elongate, brownish	12	22	---	0.33	6.0	206	0.436	0.032	0.0674	0.0008	0.48	420.7	4.8	368	22
347/21	elongate, light-orange	25	19	0.01	0.14	5.4	391	0.5108	0.0053	0.0672	0.0002	0.52	419.0	1.2	419	4
347/20	round, brownish	5	15	0.17	1.08	7.4	61	0.532	0.029	0.0695	0.0004	0.66	433.0	2.1	433	19
347/22	rectangular, olive	8	25	0.01	0.55	6.4	153	0.523	0.015	0.0692	0.0007	0.40	431.5	4.1	427	10
sample Sk3c, leucosome																
332/15	reddish	4	11	0.08	1.01	6.0	51	0.540	0.048	0.0703	0.0005	0.76	437.9	2.9	438	31
sample Sk3a, subhorizontal fabric																
332/22	reddish	3	14	---	1.04	5.1	53	0.563	0.046	0.0706	0.0005	0.74	439.7	2.8	453	30
326/15	olive	6	2.9	---	0.22	3.3	42	0.57	0.10	0.0727	0.0009	0.77	452.6	5.6	461	64
332/20	olive	6	4.1	---	0.79	6.7	36	0.609	0.084	0.0761	0.0008	0.77	472.5	4.6	483	52
332/23	black	7	0.8	---	0.48	5.4	24	0.76	0.32	0.0895	0.0027	0.67	552.4	16.1	571	170
Titanites																
sample Sk3a, subhorizontal fabric																
332-42	two clear grains	22	36	0.07	1.74	40.1	107	0.5547	0.0087	0.07100	0.00018	0.55	442.2	1.1	448.1	5.6
338/50	one clear grain	1	183	0.06	60.03	61.8	31	0.573	0.064	0.07056	0.00055	0.70	439.5	3.3	460	40
347-48	one platy light-orange grai	6	6	0.03	0.58	5.5	49	0.534	0.059	0.07046	0.00069	0.44	438.9	4.2	434	38
347-46	one long lightbrown grain	7	68	0.07	3.18	24.3	103	0.526	0.019	0.06928	0.00034	0.18	431.8	2.1	429	12
332-60	six clear grains	37	62	0.11	3.45	129.1	96	0.5383	0.0096	0.06917	0.00018	0.54	431.1	1.1	437.3	6.3
326/83	one clear grain	46	116	0.05	2.83	131.6	193	0.5242	0.0052	0.06888	0.00022	0.58	429.4	1.3	427.9	3.5
326/84	one clear grain	33	75	0.06	2.86	95.9	129	0.5221	0.0060	0.06882	0.00017	0.47	429.0	1.0	426.5	4.0
332-48	two clear grains	12	50	0.23	2.94	37.1	87	0.58	0.11	0.0683	0.0013	0.90	426.0	7.7	467	69
338/21	one clear grain	6	74	0.09	4.60	29.5	82	0.511	0.045	0.0681	0.0054	0.91	425	32	419	30

(1) weight and concentrations are known to better than 10%

(2) Pbc = initial common Pb, corrected for fractionation and blank

(3) model Th/U calculated from 206Pb/208Pb ratio and age of sample

(4) Pbcom = total common Pb in sample (initial + blank)

(5) raw data corrected for fractionation

(6) corrected for fractionation, spike, blank and initial common Pb; for rutile in samples Sk3d and Sk3c the latter was corrected using the Pb composition of plagioclase from sample Sk3c (206/204 = 18.458 +/- 0.037 and 207/204 = 15.594 +/-0.047): rutile and titanite from sample Sk3a used the 206/204 and 207/204 of coexisting plagioclase ((206/204 = 18.365 +/-0.04 and 207/204 = 15.569 +/-0.048). The error is calculated by propagating the main sources of uncertainty.